

X-ray spectral correlations in a sample of Low-mass black hole X-ray binaries in the hard state

BEI YOU,¹ YANTING DONG,² ZHEN YAN,³ ZHU LIU,⁴ YOU LI TUO,⁵ YUANLE YAO,⁶ AND XINWU CAO⁷

¹*School of Physics and Technology, Wuhan University, Wuhan, 430072, People's Republic of China*

²*Institute for Astronomy, School of Physics, Zhejiang University, 866 Yuhangtang Road, Hangzhou, 310058, People's Republic of China*

³*Shanghai Astronomical Observatory, Chinese Academy of Sciences, 80 Nandan Road, Shanghai, 200030, People's Republic of China*

⁴*Max Planck Institute for Extraterrestrial Physics, Giessenbachstrasse 1, D-85748, Garching, Germany*

⁵*Institut für Astronomie und Astrophysik, Universität Tübingen, Sand 1, D-72076 Tübingen, Germany*

⁶*School of Physics and Technology, Wuhan University, Wuhan 430072, People's Republic of China*

⁷*Institute for Astronomy, School of Physics, Zhejiang University, 866 Yuhangtang Rd, Hangzhou, 310058, People's Republic of China*

ABSTRACT

The power-law emission and reflection component provide valuable insights into the accretion process around a black hole. In this work, thanks to the broadband spectra coverage of the *Nuclear Spectroscopic Telescope Array*, we study the spectral properties for a sample of low-mass black hole X-ray binaries (BHXRBS). We find that there is a positive correlation between the photon index Γ and the reflection fraction R (the ratio of the coronal intensity that illuminates the disk to the coronal intensity that reaches the observer), consistent with previous studies, but except for MAXI J1820+070. It is quite interesting that this source also deviates from the well-known “V”-shaped correlation between the photon index Γ and the X-ray luminosity $\log L_X$, when it is in the bright hard state. More specifically, the Λ -shaped correlation between Γ and $\log L_X$ is observed, as the luminosity decreases by a factor of 3 in a narrow range from $\sim 10^{38}$ to $10^{37.5}$ erg s⁻¹. Furthermore, we discover a strong positive correlation between R and the X-ray luminosity for BHXRBS in the hard state, which puts a constraint on the disk-corona coupling and the evolution.

1. INTRODUCTION

The primary X-ray emission in X-ray binaries and active galactic nuclei (AGNs) produced via inverse Compton scattering of the soft photons in the hot compact region, often referred to as corona, is described by a power law with a high energy cutoff (Done et al. 2007; You et al. 2012; Yuan & Narayan 2014). A reflection component, which is believed to be produced by the illumination of the reflecting medium by the primary X-ray, is also observed. The reflection component is composed of fluorescent emission lines and a hump in the range of ~ 20 – 40 keV. We use the photon index Γ to describe the slope of the primary X-ray, which indicates the fraction of the energy from the soft seed photons deposited into the corona. The reflection fraction R is used to indicate the fraction of the primary X-ray intercepted by the reflection medium, namely, the relative cold disk (García et al. 2013). The correlations between the X-ray properties (e.g., Γ and broad-band luminosity L_X) and R imply the geometric and physical properties of the accretion flow around the central object (Wu & Gu 2008; Plant et al. 2014; You et al. 2021).

The positive correlation between Γ and R was found for the black hole X-ray binary (BHXRBS) GX 339-4 in the hard state by fitting *Ginga* spectra (Ueda et al. 1994). Zdziarski et al. (1999) reported a similar correlation in Seyfert galaxies and in the hard state of four binary systems, and provided evidence for the reflective medium as the dominant source for seed photons to the corona. The correlation was also studied by analyzing *RXTE/PCA* data for GX 339-4 and Cyg X-1 hard state (Gilfanov et al. 1999; Revnivtsev et al. 2001), and for the sample of low-mass X-ray binaries (LMXBs; Steiner et al. 2016). However, the physical interpretation of this correlation is still under debate, which might be either the evolution of the inner radius (Zdziarski et al. 1999; Qiao & Liu 2017; Liu & Qiao 2022) in the scenario of the truncated disk, or the bulk velocity of the corona with respect to the disk (Beloborodov 1999). As for the correlation between L_X and R , it was found that the R gradually increases as the source luminosity rises for GX 339-4 in the hard state, which was interpreted in the scenario of the truncated disk (Plant et al. 2014). However, a statistical study of the correlation between L_X and R for a sample of LMXBs is required, in order to not only verify the observational correlation but also well understand the physical origin behind this correlation.

The Nuclear Spectroscopic Telescope Array (*NuSTAR*) is the first focusing telescope above 10 keV (Harrison et al. 2013). The high signal-to-noise ratio and broad energy band provide a good opportunity to better study the primary X-ray and the reflection hump, compared to previous spectral studies (Diaz et al. 2020; Draghis et al. 2020; Connors et al. 2021; Marino et al. 2021; Tripathi et al. 2021; Feng et al. 2022; Prabhakar et al. 2022; Rout et al. 2022). The correlation between Γ and R by analysing *NuSTAR* spectra has been recently reported for Seyfert galaxies (Ezhikode et al. 2020; Panagiotou & Walter 2020) and radio galaxies (Kang et al. 2020).

The motivation of this work is to statistically study the correlations between the X-ray properties (Γ and L_X) and R , in a sample of stellar-mass black hole systems in the hard state, using *NuSTAR* archived data. This paper is organized as follows. In section 2, we present the sample selection and data reduction. In section 3, we give the spectral analysis and the best-fit results. Finally, the discussions and conclusions are presented in section 4.

2. SAMPLE AND DATA REDUCTION

In this work, we adopt the *NuSTAR* sample of 17 LMXBs which is constructed by Yan et al. (2020), consisting of 165 observations downloaded from *HEASARC*. The data reduction was performed through the *NUPIPELINE* task of *NUS-TARDAS* included in *HEASOFT* 6.29.

We set `saamode=optimized` and `tentacle=yes` to filter passages through the South Atlantic Anomaly, and set `arfmllicorr=yes` to correct the temperature dependence of the multilayer insulation (MLI) for the FPMA data (Madsen et al. 2020). For the bright sources, we use `STATUS==b0000xxx00xxx000` to reprocess the data¹. *CALDB* version 2021115 is used for the calibration. We extract the source spectra within a uniform radius of 90'' at the source position, and the background spectra within an annulus defined between 180'' and 200''.

An overview of all data is presented in Figure 1, in which the observation of 4U 1630-472 on MJD 56723 (30001016002) and the observation of H1743-322 on MJD 57251 (80002040006) are excluded, due to the spectra being dominated by the background. We plot the count rate within 3–78 keV and the hardness ratio (HR) defined as the 10–78 keV count rate divided by the 3–10 keV count rate in the upper and lower panels, respectively. In this work, we aim to study the correlations between the X-ray primary and the disk reflection of LMXBs in the hard state. We set $HR > 0.3$ as the selection criterion for the hard state. In this condition, observations of 4U 1630-472, MAXI J1631-479, and V4641 Sgr are excluded. Furthermore, we also exclude ob-

servations for which the spectral fits do not require the reflection component, in the sense that those spectra can be well described by an absorbed power-law model, or an absorbed power-law plus `diskbb` model.

Additionally, the observations of V404 Cyg on MJD 57198 (ObsID: 90102007002) and MJD 57199 (ObsID: 90102007003), and GRS 1915+105 on MJD 58608 (ObsID: 90501321002) and MJD 58623 (ObsID: 30502008002), are excluded, the spectra of which are quite complex and cannot be well fitted in our preliminary analysis with the reflection model ($\chi^2_\nu \gg 2$). For V404 Cyg in the 2015 outburst, strong flares were observed, which were thought to be related to transient jet activity of ejecting plasma close to a BH. The corresponding spectral fitting to the *NuSTAR* observations on MJD 57198 and 57199 suggested that an X-ray source is close to a BH with a height smaller than $6 R_g$ and its spectra are extremely hard with $\Gamma \sim 1.4$ (Walton et al. 2017). For GRS 1915+105, the *NuSTAR* observations indicated that it was also in the flaring state on MJD 58608 and 58623, given the clear detection of the absorption features in the spectral residual, which were attributed to the accretion disk winds (Koljonen & Tomsick 2020; Aramburu Sanchez et al. 2020). Therefore, the final sample in this work is composed of 12 LMXBs with 69 observations in total. Detailed information is provided in Table 1 and Table 2.

3. SPECTRAL ANALYSIS

We perform the spectral fitting in *XSPEC* 12.11.1 (Arnaud 1996). We account for the Galactic absorption using `TBabs` (Wilms et al. 2000). The column density (N_H) was fixed to the values presented in Table 1, most of which are obtained from the previous *NuSTAR* spectral analysis in the literature. We adopt a relativistic reflection model `relxillCp` (García et al. 2013; Dauser et al. 2014; García et al. 2014), to account for the reprocessed emission between the disk and corona. This reflection model contains both the direct Comptonization from the corona and its reflection on the disk. Therefore, `TBabs*relxillCp` in *XSPEC* notation, is used to fit spectra in our sample. A possible disk component (`diskbb`) and a nonrelativistic reflection model `xillverCp` will be added if they can significantly improve the fitting. The non-relativistic reflection component `xillverCp` may originate from the distant disk reflection. So, the ionization parameter is fixed at a low value with $\log \xi = 0.5$, for simplicity. And the Comptonization parameters (the electron temperature and the photon index) in `xillverCp` are linked to the ones in `relxillCp` (Buisson et al. 2019; You et al. 2021). Note that, for the reflection model `relxillCp`, no specific geometry of the Comptonization source is assumed, but with an artificial broken power-law emissivity. Alternative reflection models with significant findings of spectral complexity

¹ <https://heasarc.gsfc.nasa.gov/docs/nustar/analysis/>

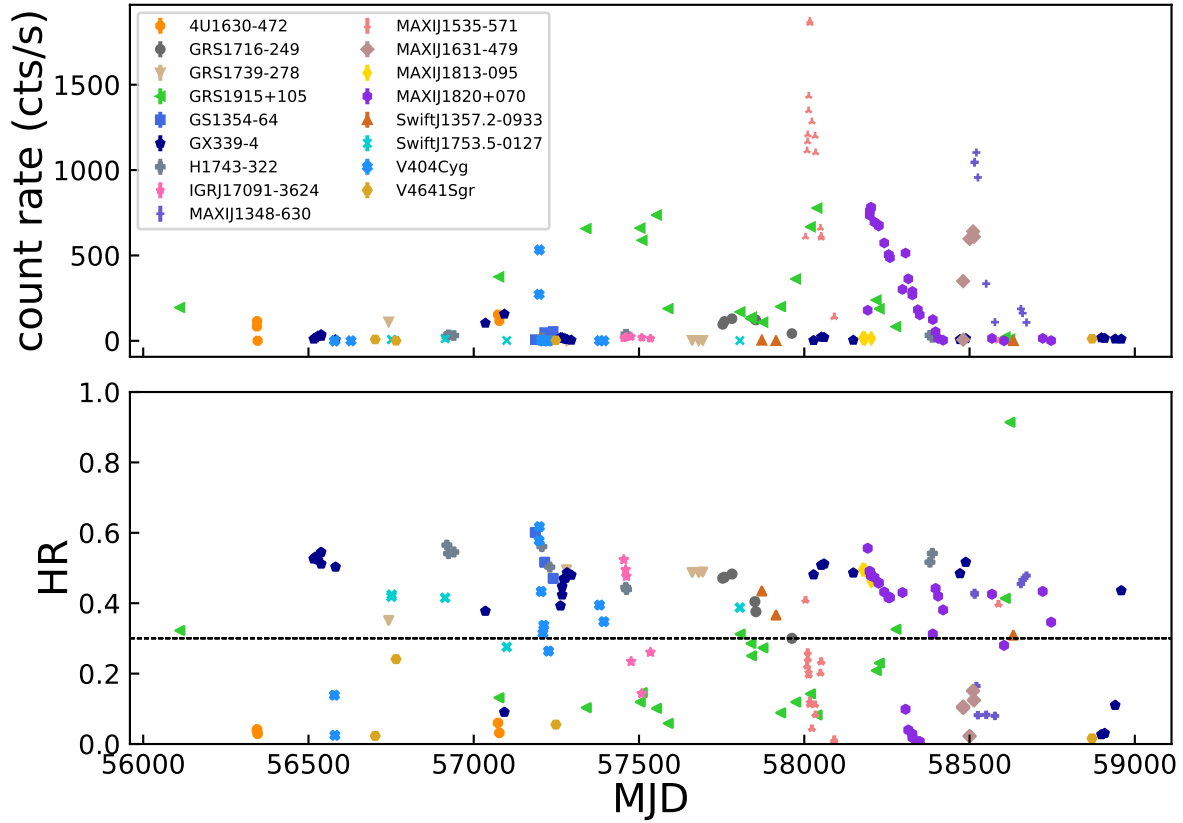


Figure 1. Overview of all observations, except the observation of 4U 1630-472 on MJD 56723 and the observation of H1743-322 on MJD 57251 due to background counts dominating their spectra. The net count rate within 3–78 keV and HRs are shown in the upper and lower panels, respectively. The HR is defined as the count rate within the energy band of 10–78 keV divided by the count rate within 3–10 keV. Here, we only show an overview of FPMA for clarity.

are also available in the literature (Mahmoud & Done 2018; Zdziarski et al. 2021a,b; Kawamura et al. 2022).

As for `relxillCp`, the inclination angle i is left free in the spectral fitting, except GRS 1915+105, MAXI J1820+070, and GX 339-4. The inclination angles of the first two sources are adopted from the measurements of jet inclination angles (Reid et al. 2014; Atri et al. 2020), i.e., $i = 60^\circ$ for GRS 1915+105 and $i = 63^\circ$ for MAXI J1820+070. However, we notice that there is a large misalignment ($> 40^\circ$) between the inclination angles of the jet and binary orbit in MAXI J1820+070 (Poutanen et al. 2022). As for GX 339-4, the binary inclination is constrained to be $37^\circ < i < 78^\circ$ from the VLT/X-shooter observations. Moreover, as suggested by Zdziarski et al. (2019), the inclination of this source is unlikely to be high, which is supported by the absence of the disk winds (Ponti et al. 2012) and the track on the hardness–intensity diagram (Muñoz-Darias et al. 2013). In the preliminary spectral fits of GX 339-4, the inclination is pegged at a lower limit. Therefore, the inclination angle

of this source is fixed at $i = 40^\circ$ in the following fits. In this work, we aim at determining the connection between the corona and accretion disk, while the robust estimate of the BH spin a_* for an individual source of the sample is beyond the scope of this paper. Therefore, for simplicity, we fix the BH spin $a_* = 0.998$ for the *NuSTAR* sample here. The photon index Γ , reflection parameter R , the electron temperature kT_e , the iron abundance A_{Fe} and normalization were free parameters in the spectral fits.

For a given source, the two free parameters, i.e., the inclination of the binary system and the Fe abundance of the accretion disk, are expected to be constant. Therefore, we perform joint fits to multi-epoch spectra for a given source, in the sense that the two parameters between the multi-spectra are linked. Given that (i) the complexity in configuring the `xcm` files for the joint fits with the complex reflection model, and (2) the reported rip occurring in early 2016 in the MLI associated with FPMA, which resulted in an increased pho-

Table 1. Basic information on the BXRBs

Source	N_{H} (10^{22} cm^{-2})	Inclination ($^{\circ}$)	Mass (M_{\odot})	Distance (kpc)	Ref.
GRS 1716-249	0.6	-	-	6	[1] - - [2]
GRS 1739-278	2.3	-	-	7.5	[3] - - [4]
GRS 1915+105	6.11	60 ± 5	12.4	8.6	[5] [6] [6] [6]
GS 1354-64	0.7	≤ 79	7.6	7	[7] [8] [8] [9]
GX 339-4	0.41	37-78	5.9	9	[10][11][11][11]
H1743-322	2.3	-	-	8.5	[12][13] - [13]
IGR J17091-3624	1.59	-	-	12	[14] - - [27]
MAXI J1348-630	0.86	-	-	2.2	[15] - - [16]
MAXI J1535-571	5.5	-	-	4.1	[17] - - [18]
MAXI J1813-095	0.82	-	-	6	[19] - - [26]
MAXI J1820+070	0.15	63 ± 3	8.48	2.96	[20][21][28][21]
Swift J1753.5-0127	0.2	≥ 40	7.4	8.42	[22][23][24][25]

[1]Bharali et al. (2019); [2]Saikia et al. (2022); [3]Miller et al. (2015); [4]Yan & Yu (2017); [5]Miller et al. (2013); [6]Reid et al. (2014); [7]El-Batal et al. (2016); [8]Casares et al. (2009); [9]Gandhi et al. (2019); [10]Wang-Ji et al. (2018); [11]Heida et al. (2017); [12]Chand et al. (2020); [13]Steiner et al. (2012); [14]Xu et al. (2017); [15]Chakraborty et al. (2021); [16]Chauhan et al. (2021); [17]Dong et al. (2022); [18]Chauhan et al. (2019); [19]Jiang et al. (2022); [20]Uttley et al. (2018); [21]Atri et al. (2020); [22]Shaw et al. (2016b); [23]Neustroev et al. (2014); [24]Shaw et al. (2016a); [25]Gandhi et al. (2019); [26]Jana et al. (2021); [27]Iyer et al. (2015); [28]Torres et al. (2020)

ton flux in FPMA spectra of bright sources ², we will only use the FPMB spectra in the energy band of 3–78 keV, for each observation. For MAXI J1820+070, due to the complex fitting model (the disk component, the relativistic reflection and the nonrelativistic reflection) and there being 18 spectra in total, we divide these spectra into two data sets: one for the rising hard state before MJD=58303, and the other one for the decaying hard state after MJD = 58303 (Buisson et al. 2019). The iron abundance of the second data set is fixed at the best-fitting value of the second data sets, in order to keep this parameter constant during the outburst in 2018.

The best-fitting results are obtained by implementing a Markov Chain Monte Carlo (MCMC) algorithm in XSPEC to create a chain of parameter values whose density gives the probability distribution for that parameter. The analysis of the probability distributions derived from the MCMC chains is implemented using the corner package Foreman-Mackey et al. (2013). The best-fit results for each free parameter are taken as the medians of the corresponding posterior distributions, and the error bars correspond to the 68% confidence interval (1σ uncertainty).

The best-fitting results are presented in Table 3. Once the best-fitting result is derived, we then use the convolution model *cflux* to estimate the unobserved 3–78 keV X-ray fluxes of the *relxillCp* component.

4. RESULTS AND DISCUSSION

4.1. Disk-Corona Relation

The hard X-ray from the corona illuminates the disk, which is reprocessed within the disk to produce the reflection spectrum (George & Fabian 1991; García et al. 2013; You et al. 2021; Klepczarek et al. 2023). Therefore, the reflection spectrum is a crucial ingredient to study the relation between the corona and disk (You et al. 2021). We then explore the disk-corona relation through the correlations between different spectral parameters.

4.1.1. The Γ - R relation

For GRS 1739-278 and Swift J1753.5-0127, the spectra can be well fitted by a simple Comptonization model *nthcomp* (Zdziarski et al. 1996) without the presence of the reflection features. This means the reflection fraction cannot be well constrained by the data. Therefore, excluding these two sources, we examine the correlation between R and Γ using Spearman rank-order test. In order to take into account uncertainties of the parameters, we perform Monte Carlo sampling of the R and Γ (Curran 2014). We notice that some observations of MAXI J1820+070 apparently deviate from this correlation with a large scatter. The complexity of this source will be discussed below. If MAXI J1820+070 is excluded from the sample, we obtain a correlation between R and Γ , with the Spearman’s coefficient of 0.53 at a significance of 3.78σ .

Furthermore, in order to better understand the physical origin of the correlation, we need to derive the form of the correlation. Zdziarski et al. (1999) studied the correlation between Γ and the R by fitting a few phenomenological functions to the data. And, they found that the best model is a power law, $R = u\Gamma^{\nu}$ with $u = (1.4 \pm 1.2) \times 10^{-4}$, $\nu = 12.4 \pm 1.2$. Here, we use the *linmix* algorithm (Kelly 2007) imple-

² https://heasarc.gsfc.nasa.gov/docs/nustar/nustar_faq.html#MLI

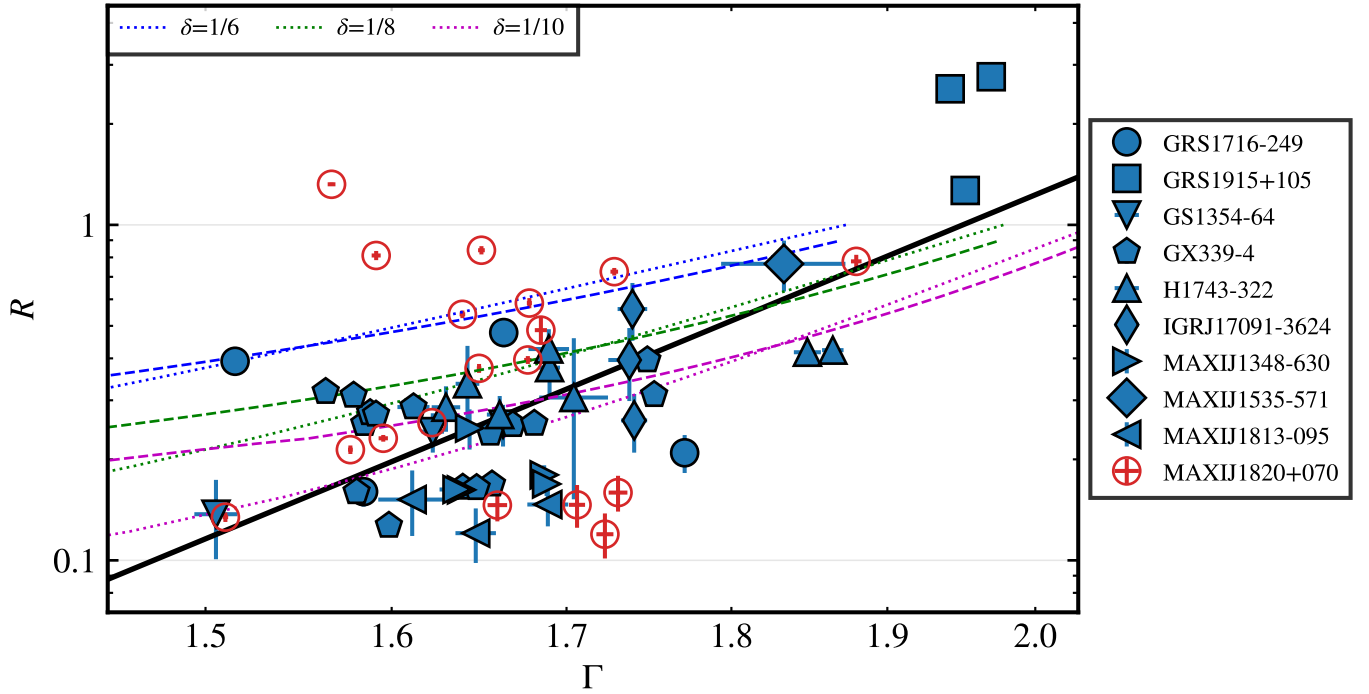


Figure 2. The relationship between Γ and R . GRS 1739-278 and Swift J1753.5-0127 are not included, due to that the spectra can be well fitted by a simple Comptonization model without the presence of the reflection features. The solid line denotes the best-fitting result excluding MAXI J1820+070 (open red circle). We also calculate the relationship between Γ and R based on the models proposed by Zdziarski et al. (1999, shown in dotted lines) and Beloborodov (1999, shown in dashed lines). The blue, green, and purple colors correspond to $\delta = 1/6$, $\delta = 1/8$, and $\delta = 1/10$, respectively, in Eq. (2).

mented in Python³ to fit the above correlation with a linear function $\log R = \nu \times \log \Gamma + u$. The best-fitting results are $\nu = 8.20 \pm 1.20$, $u = -2.38 \pm 0.27$ (see also Figure 2).

The reflection fraction could be approximated as the ratio of the luminosity of the primary X-ray source with unit luminosity incident on the disk to the one radiated outward to infinity,

$$R = L_d / (1 - L_d), \quad (1)$$

where L_d is the incident luminosity over the disk (Zdziarski et al. 1999). And the photon index Γ can be estimated from the Compton amplification factor of the thermal Comptonization A (Beloborodov 1999),

$$\Gamma \approx 2.33(A - 1)^\delta. \quad (2)$$

The Compton amplification factor is defined as $A \equiv 1/L_s$, where L_s is the power in seed photons scattered in the sphere (assuming a unit optical depth).

In the scenario of the truncated disk, both the reflection fraction R and the Compton amplification factor A depend on the disk truncation radius d , which can be estimated from Eq. (1) and (2) of Zdziarski et al. (1999). In the scenario of the outflowing X-ray source, assuming the geometry is

steady, both R and A also depend on the outflowing velocity of the corona, which can be determined from Eq. (3) and (7) of Beloborodov (1999). We plot the predicted correlations between R and Γ for these two scenarios, in the case of $\delta = 1/6$, $\delta = 1/8$, and $\delta = 1/10$ (see the dotted and dashed lines). It can be seen that both scenarios predict positive correlations between R and Γ , which are qualitatively consistent with the observed correlation (except for MAXI J1820+070) in the *NuSTAR* sample.

Some observations of MAXI J1820+070 apparently deviate from the positive R - Γ correlation above. It seems that there is a negative correlation between R and Γ in MAXI J1820+070. We notice that *Insight*-HXMT also monitored this source with higher cadence and in a broader energy band (2–150 keV) during the outburst in 2018, which was comprehensively studied in You et al. (2021). In order to study the evolution of MAXI J1820+070, we also plot the Γ and R obtained from You et al. (2021) in Figure 3.⁴ Combining the results from both *NuSTAR* and *Insight*-HXMT, it is evident

⁴ At the time of preparing the publication of You et al. (2021), *relxill* v 1.4.0 was the latest available version, with the bug fixed in v 1.4.3, see <http://www.sternwarte.uni-erlangen.de/~dauser/research/relxill/>. In this work, using the latest version of *relxill*, the spectral fits to *Insight*-HXMT spectra are updated.

³ <https://github.com/jmeyers314/linmix>

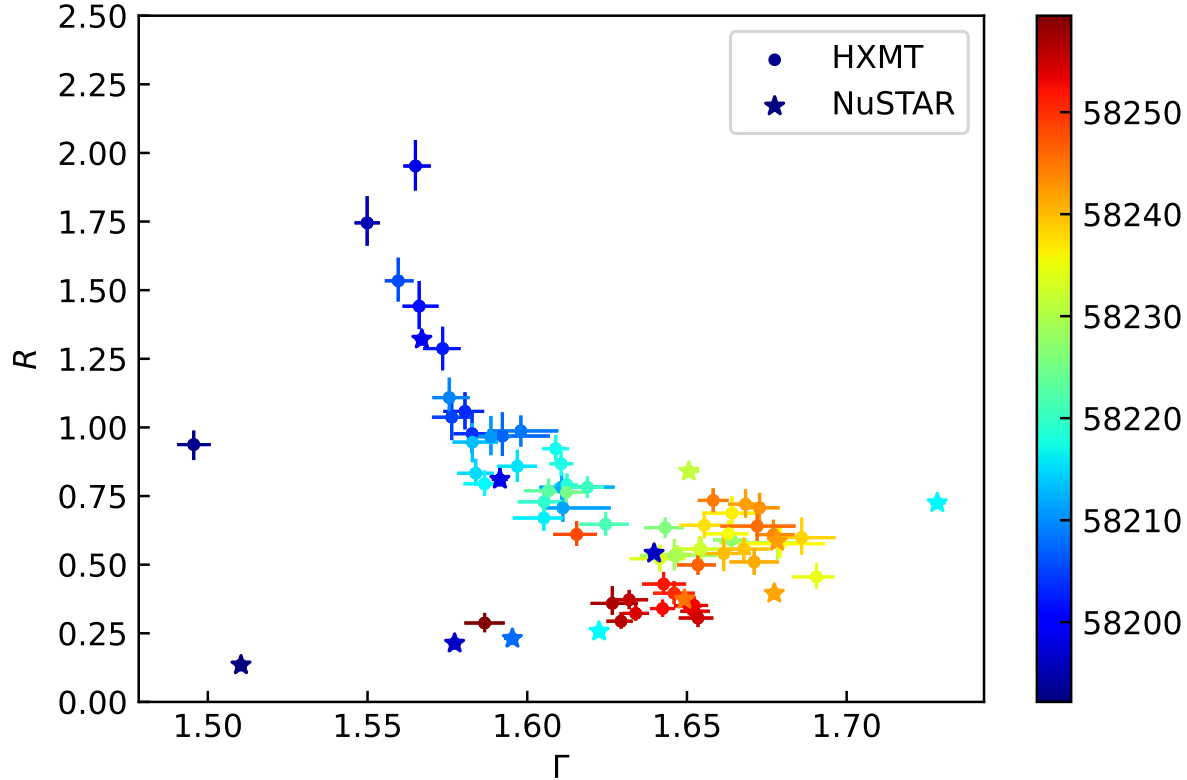


Figure 3. The relationship between Γ and R for MAXI J1820+070 in the rising hard state during the outburst rise in 2018 (before MJD = 58303), in which the estimations from the spectral fitting to both *NuSTAR* (blue points) and *Insight-HXMT* (red points) observations are included. The color of each point corresponds to the observation MJD, with the color bar on the right.

that (i) the reflection fraction is indeed large and can reach up to ~ 2 during the peak of the rising hard state (around MJD 58200); (ii) there is indeed a negative correlation, where the reflection fraction rapidly decreases from ~ 2.0 to 0.25, as Γ increases in a narrow range from 1.55 to 1.7. The Spearman coefficient is -0.59 at a significance of 5.88σ .

4.1.2. The R - L_X correlation

We then study the possible correlation between R and $\log L_X$ for this *NuSTAR* sample. The Spearman coefficient of the correlation between R and L_X is 0.66 at a significance of 5.02σ . This positive correlation can be explained in the truncated disk model. It is hard to directly compute the Comptonization luminosity L_C , but it is proportional to the luminosity L_S of the seed photons which are scattered in the X-ray source, i.e., $L_C \propto L_S$ (Poutanen et al. 2018). The reflection fraction R is computed with Equation (1), and L_S is computed using Equations (1) and (2) of Zdziarski et al. (1999). L_S is a function of the truncation radius d of the accretion disk. The model prediction of the R - L_X correlation is plotted in Figure 4, as a dashed line. The observations roughly follow the

model prediction below $\sim 5 \times 10^{37} \text{ erg s}^{-1}$, and apparently deviate from it at higher luminosity.

The positive correlation between R and L_X for MAXI J1820+070 is much more evident than the one for the sample study above. For clarity, we plot the estimates R and $\log L_X$ in Fig. 5, including the results of both *NuSTAR* and *Insight-HXMT* during the rising hard state of the outburst in 2018. It can be seen that these combined estimates do show a positive correlation, with the reflection fraction rapidly increasing over one order of magnitude as the luminosity increases by a factor of 3. The Spearman coefficient is 0.8 at a significance of 9.4σ .

In the truncated disk model (Esin et al. 1997; Done et al. 2007; Qiao & Liu 2012), it is proposed that the outer disk truncation radius decreases with the mass accretion rate, which leads to the softening of the spectrum. If assuming the inner Comptonization source (i.e., advection-dominated accretion flow) is static, the reflection fraction will increase with the mass accretion rate (i.e., the luminosity), given that the reflection fraction increases as the truncation radius decreases (Zdziarski et al. 1999). Plant et al. (2014) carried out

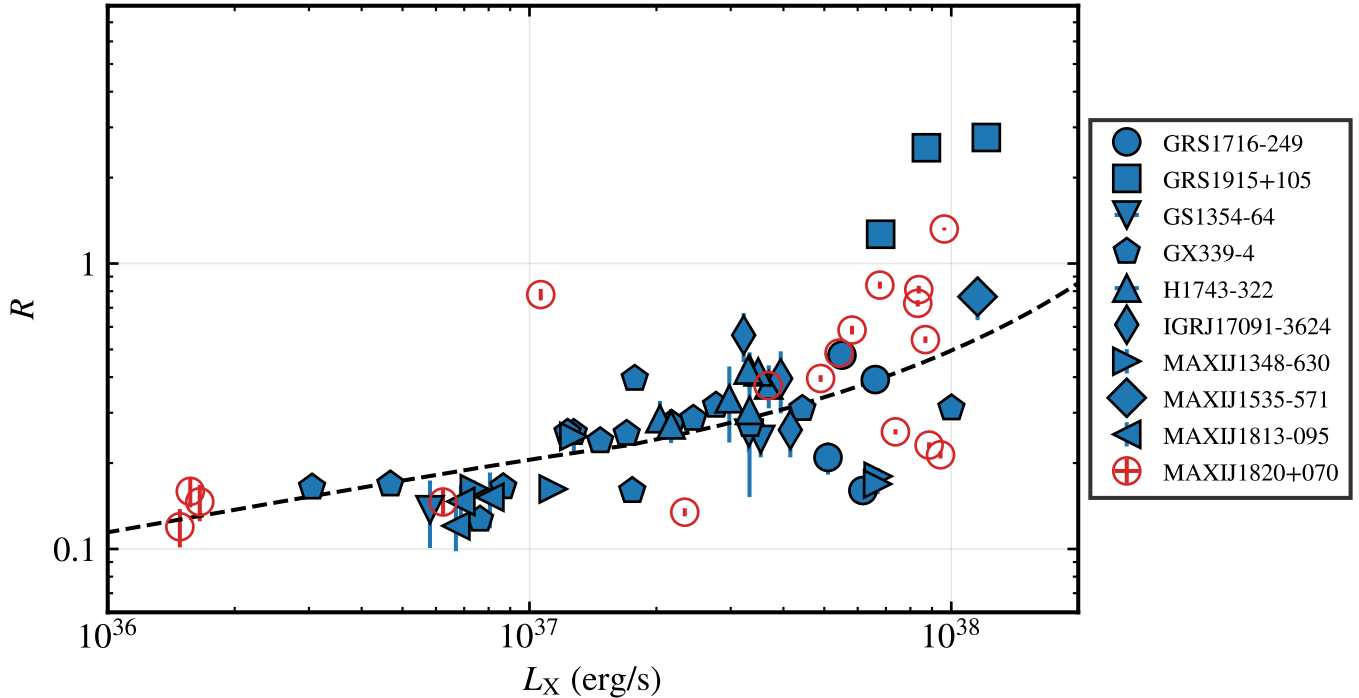


Figure 4. Correlation between R and the X-ray luminosity L_X of the `relxillCp` component in 3–78 keV for the *NuSTAR* sample. GRS 1739-278 and Swift J1753.5-0127 are not included, due to that the spectra can be well fitted by a simple Comptonization model without the presence of the reflection features.

a systematic analysis of the reflection spectrum throughout three outbursts of GX 339-4. It was found that R gradually increases as the source luminosity for this source in the hard state, which was interpreted in the scenario of the truncated disk. In [De Marco et al. \(2017\)](#), the X-ray reverberation lags in GX 339-4 were measured in the hard state, which were found to decrease as a function of X-ray luminosity. In the truncated disk model, the decrease in the lag amplitude suggests a decrease in the relative distance between the disk and corona, which may lead to an increase in the reflection fraction. Therefore, the positive correlation L_X - R derived in this work, is consistent with previous spectral and timing studies. Recently, in [Sridhar et al. \(2020\)](#), the *RXTE* observations of GX 339-4 in the 2002 and 2004 outbursts were reanalysed. They found that the reflection strengths in the 2002–2003 outburst with high X-ray flux is larger than the ones in the 2004–2005 outburst with low X-ray flux (see their Tables 2 and 3).

4.1.3. The R_{in} - L_X correlation

In this work, the disk inner radius is estimated from the spectral fits with the reflection model. In Figure 6, we plot the evolution of the disk inner radius with the X-ray luminosity of the reflection model in 3–78 keV, which shows that the disk is truncated in the hard state. We fit the correlation with the linear function Eq. (3), by replacing the X and Y with $\log L_X$ and $\log R_{in}$ and excluding all the lower limits of R_{in} .

The best-fit result is plotted as the solid line. The best-fitting slope is -0.12, which indicates a negative correlation. The Spearman coefficient of the correlation for the data is -0.04 at the significance of 0.25σ . Due to the large scatter, we cannot draw a conclusion that a negative correlation between R and L exists among the sample.

By recalibrating the *RXTE* data to a better precision, [García et al. \(2015b\)](#) reanalyzed six composite *RXTE* spectra of GX 339-4 in the hard state, with the luminosity spanning by one order of magnitude. The reflection model `relxill` was used to measure the inner disk radius. They found that the disk is slightly truncated by a few gravitational radii R_g at a few percent of Eddington, and the disk inner radius tends to decrease with the source luminosity. The same conclusion of the evolution of the disk inner radii with the source luminosities for GX 339-4 was also drawn in [Plant et al. \(2015\)](#). Recently, the same timing analysis was also applied to MAXI J1820+070 by [De Marco et al. \(2021\)](#). It was found that the frequency of thermal reverberation lags steadily increases during the outburst in 2018, implying that the relative distance between the X-ray source and the disk decreases (i.e., the decrease of the inner radius of the disk) as the source softens.

In this work, the disk component is required in the spectral fits to the *NuSTAR* data for some of the sources in the sample, e.g., MAXI J1820+070. The inner radius can also be estimated from the normalization of the `diskbb` ([Kubota et al. 1998](#)). However, in the spectral fits to *Insight*-HXMT

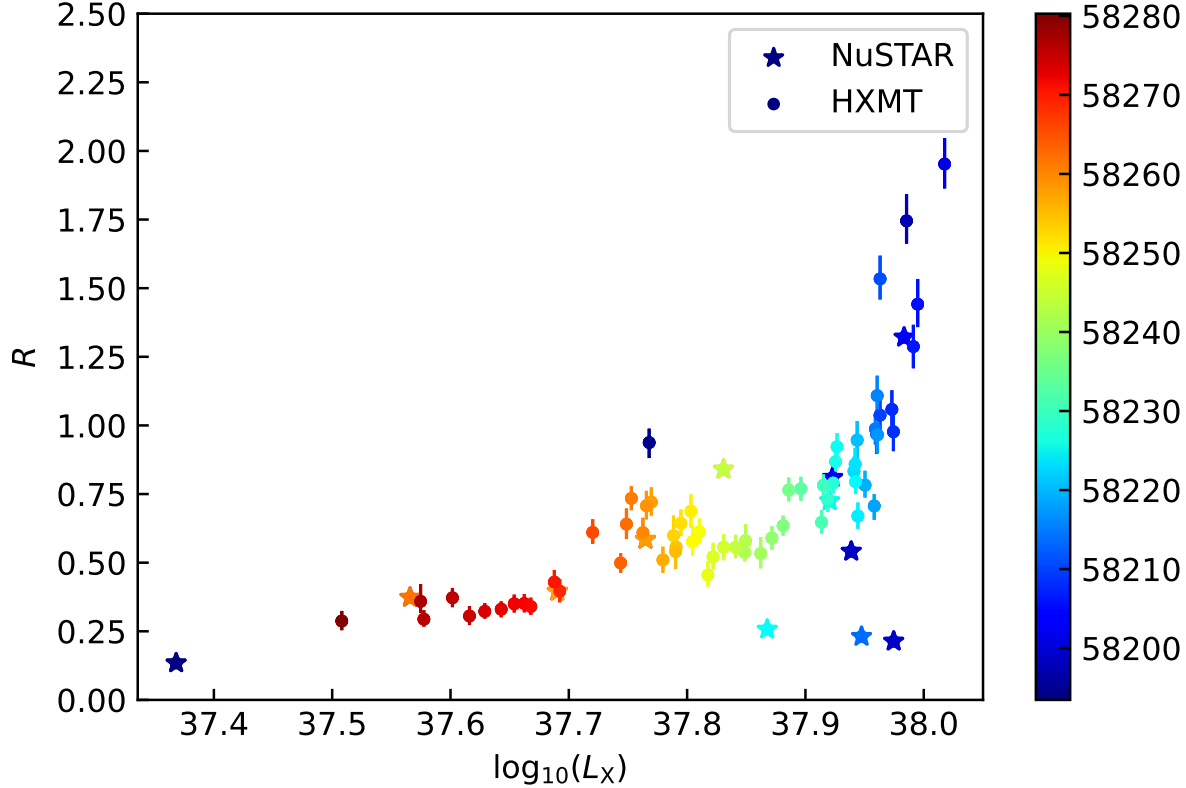


Figure 5. Correlation between R and the X-ray luminosity L_X of the `relxillCp` component in 3–78 keV for MAXI J1820+070 in the rising hard state during the outburst rise in 2018 (before MJD = 58303), in which the estimates from the spectral fits to both *NuSTAR* (star points) and *Insight*-HXMT (circle points) observations are included. The color of each point corresponds to the observation MJD, with the color bar on the right.

observations of MAXI J820+070, the estimated R_{in} from the `diskbb` components is larger than the ISCO, while the disk inner radius is fixed at ISCO (You et al. 2021) in the relativistic reflection model, based on the spectral/timing results in Kara et al. (2019). Such a disagreement would indicate that the `diskbb` components are only phenomenological descriptions of the complex spectra (Zdziarski et al. 2022b). More importantly, the estimate of R_{in} from the `diskbb` component also strongly depends on the boundary condition and the color hardening factor (Kubota & Makishima 2004; Sridhar et al. 2020; Zdziarski et al. 2022a).

4.2. Luminosity-dependent corona properties

4.2.1. Γ - L_X Correlation

In this work, we do the spectral fitting for the *NuSTAR* sample of LMXBs using the relativistic reflection model. The broadband luminosity and the corona properties, including the electron temperature and the photon index, can be well measured, so that we could statistically study the dependence of the corona properties on the X-ray luminosity. For the ac-

creting BH sources (including AGNs and BHXRBs), it was found that there is a “V”-shaped correlation between the photon index Γ and $\log L_X$ (Yamaoka et al. 2005; Wu & Gu 2008; Yang et al. 2015; Yan et al. 2020), i.e.,

$$Y(X) = \begin{cases} f_1(X - X_c) + Y_c & (X \leq X_c), \\ f_2(X - X_c) + Y_c & (X \geq X_c). \end{cases} \quad (3)$$

In this work, we investigate this correlation for the *NuSTAR* sample of LMXBs. The derived Γ and $\log L_X$ from the spectral fitting are plotted in Fig. 7. Apparently, there is also a “V”-shape correlation between Γ and $\log L_X$. Following Yan et al. (2020), we fit the correlation with the broken linear function Eq. (3), by replacing the X and Y with $\log L_X$ and Γ . The best-fit result is plotted as the solid line in Fig. 7. The correlation is broken at the luminosity $\log L_X = 37.35$, below which the slope is -0.06 , and above which the slope is 0.29 . The Spearman coefficients of the correlation for the data below and above this broken luminosity are -0.30 and 0.39 at the significances of 1.43σ and 1.91σ , respectively.

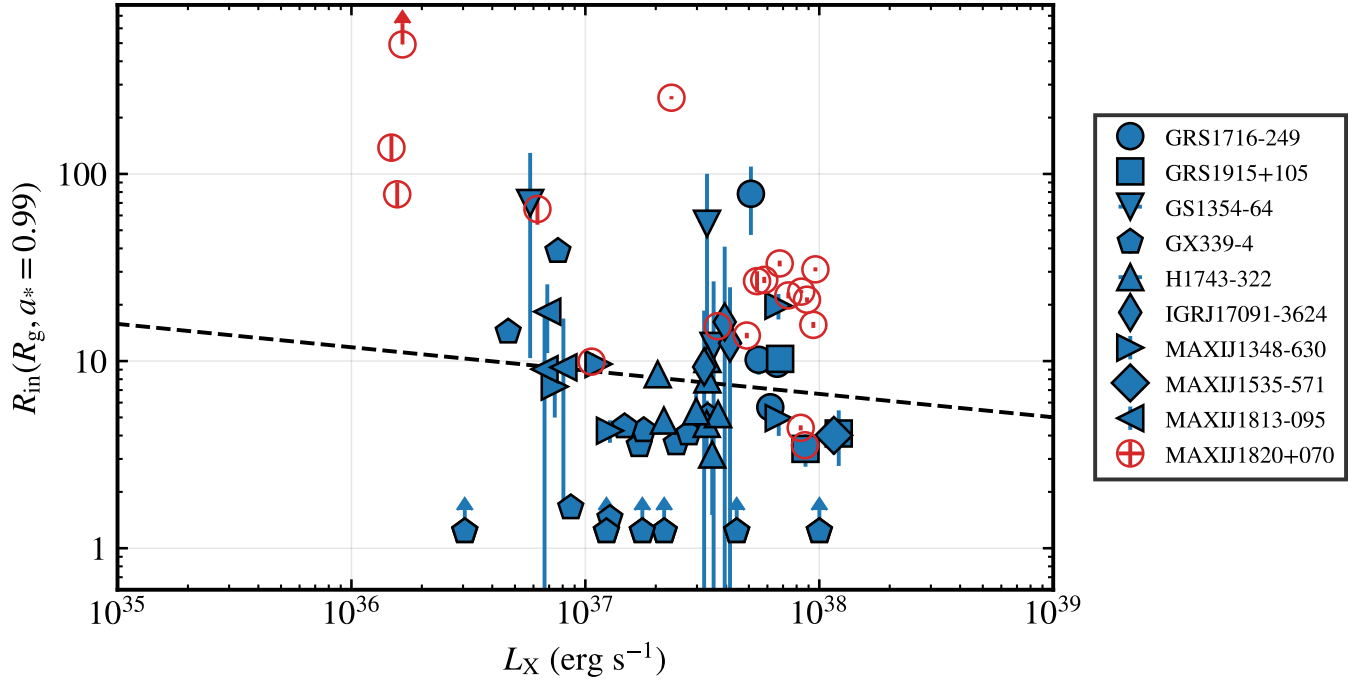


Figure 6. Correlation between R_{in} and the X-ray luminosity L_X of the *relxillCp* component in 3–78 keV for the *NuSTAR* sample. GRS 1739-278 and Swift J1753.5-0127 are not included, due to that the spectra can be well fitted by a simple Comptonization model without the presence of the reflection features.

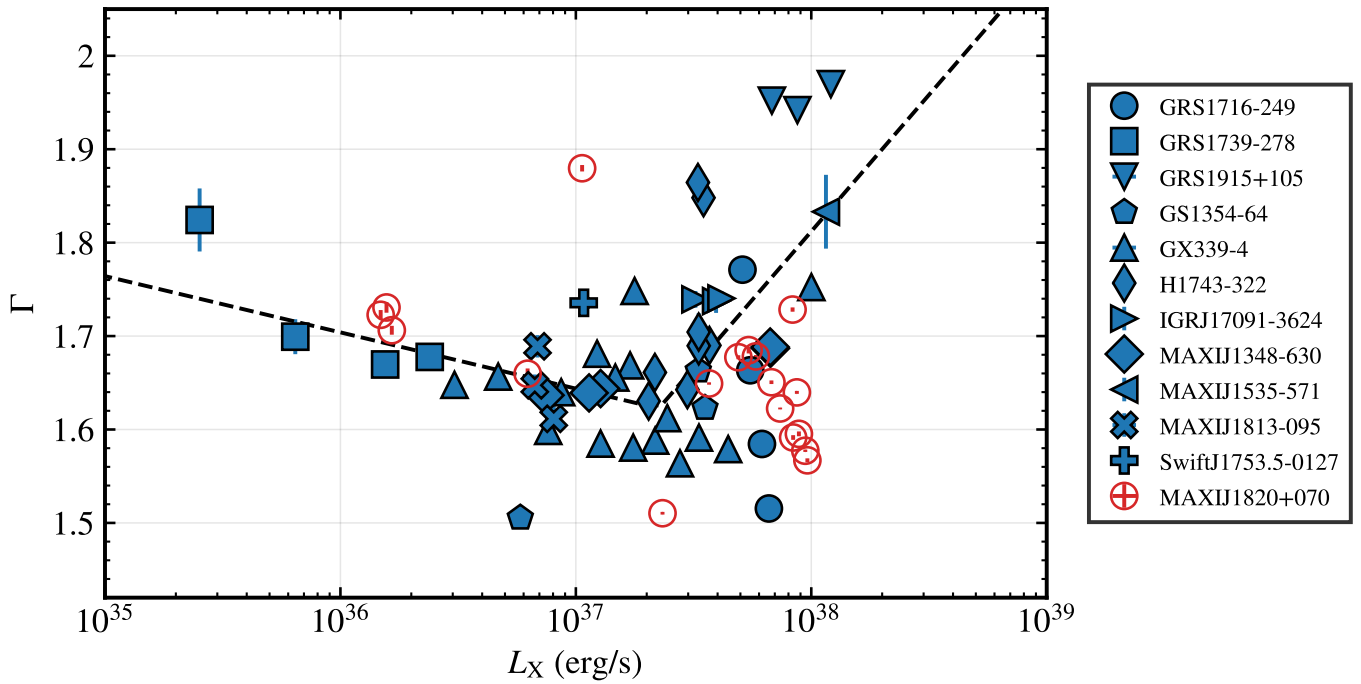


Figure 7. Correlation between photon index Γ and the X-ray luminosity L_X of the *relxillCp* component in 3–78 keV for the *NuSTAR* sample. The different colors and symbols indicate the different sources, just the same as the figure legend in Figure 1

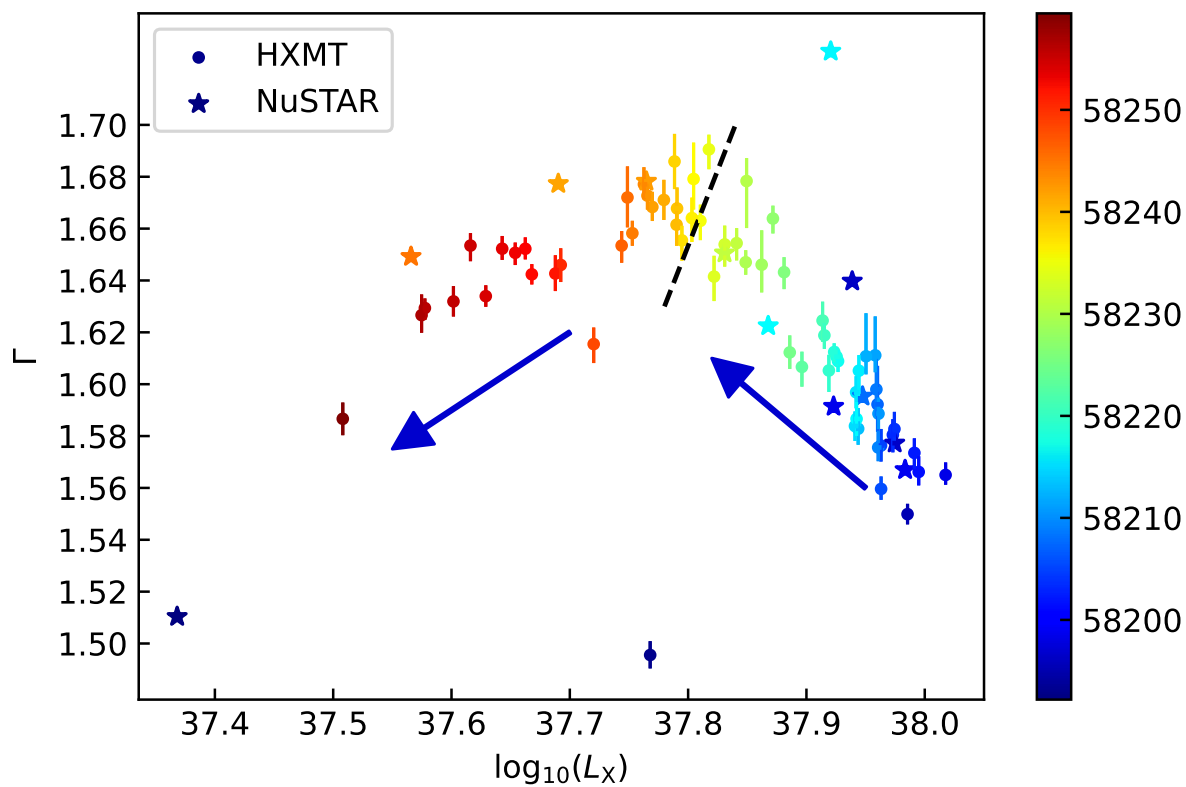


Figure 8. The relationship between Γ and the X-ray luminosity L_X of the *relxillCp* component in 3–78 keV for MAXI J1820+070 in the rising hard state during the outburst rise in 2018 (before MJD = 58303), in which the estimates from the spectral fits to both *NuSTAR* and *Insight*-HXMT observations are included. The color of each point corresponds to the observation MJD, with the color bar on the right. The dashed line roughly corresponds to MJD = 58250.

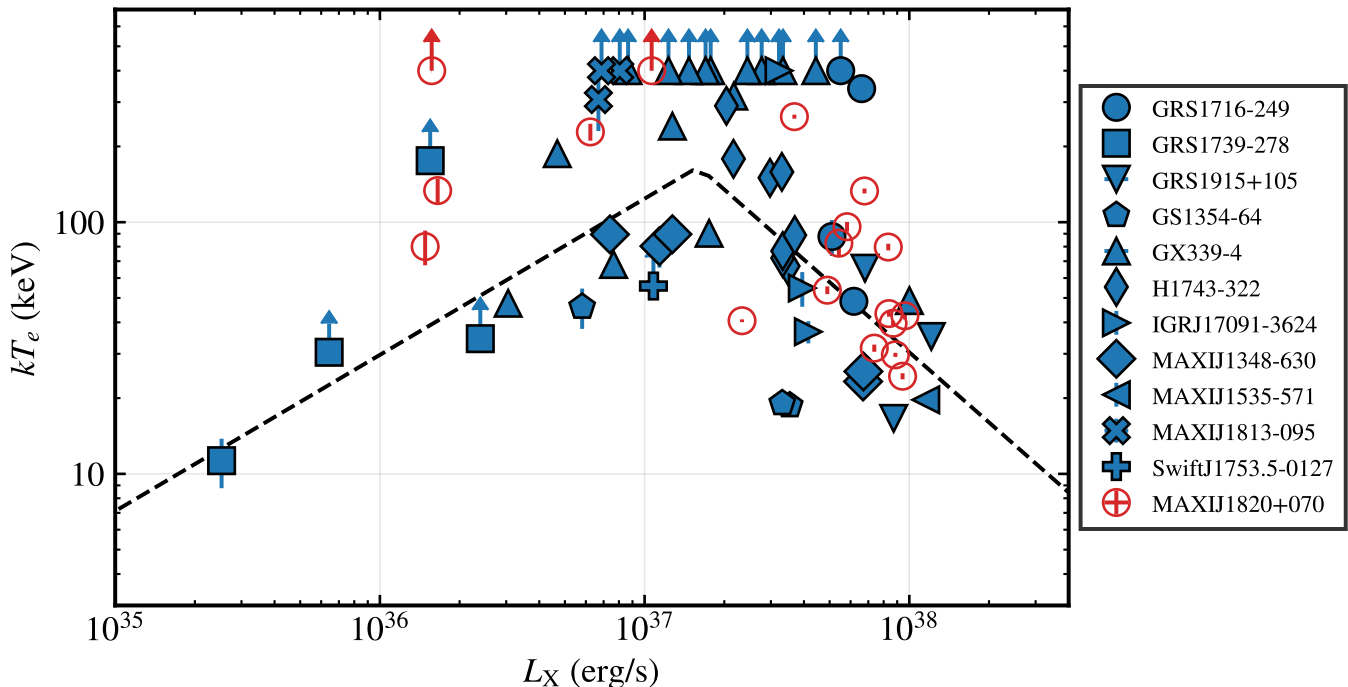


Figure 9. Correlation between the electron temperature kT_e and the X-ray luminosity L_X in 3–78 keV for the *NuSTAR* sample.

Due to the larger scatter between different sources, the negative/positive correlation below/above the broken luminosity are not very significant. This is consistent with previous studies on AGNs and BHXRBs (Wu & Gu 2008; Yang et al. 2015; Yan et al. 2020).

In Fig. 8, we plot the estimates Γ and $\log(L_X)$ from both this work and You et al. (2021), for MAXI J1820+070. Meanwhile, we associate each data point with the corresponding MJD, indicated as the color bar on the right. It can be seen that the *NuSTAR* results are consistent with the *Insight-HXMT* ones. More importantly, we notice an interesting “ Λ ”-shaped correlation between the photon index Γ and $\log L_X$, as the luminosity decreases by a factor of 3 in the narrow range from $\sim 10^{38}$ to $10^{37.5}$ erg s $^{-1}$. More specifically, Γ firstly increases as L_X decreases. But, after around MJD = 58250 (see the dashed line in Fig. 8), Γ starts to decrease as L_X continually decreases. We note that Wang et al. (2020b) studied the evolution of the temporal properties of MAXI J1820+070 over the same time with *Insight-HXMT* data sets. They also found the different behaviors of the HR, the fractional rms, and time lag before and after MJD 58,257, which suggests a transition occurred around this point.

4.2.2. kT_e - L_X Correlation

It was also found that there is a “ Λ ”-shaped correlation between the electron temperature kT_e and $\log L_X$ (Yan et al. 2020). Note that Yan et al. (2020) were not aimed at deriving the exact value of kT_e , but instead at the trend of the kT_e - L_X correlation. So the spectral fitting was simply carried out

by the use of the Comptonization model (nthcomp) without considering the role of the reflection component. This is acceptable for the low-luminosity regime $< 10^{37}$ erg s $^{-1}$, since the reflection emission in this case is systematically weak (Fürst et al. 2016; Beri et al. 2019). However, the estimate of kT_e is probably affected by the relativistic reflection components, for the high-luminosity regime $> 10^{37}$ erg s $^{-1}$, which is covered by the sample in this work (Fabian et al. 2015; García et al. 2015a). Therefore, it is essential for us to revisit the kT_e - L_X correlation using the measurements from the spectral fitting with the relativistic reflection model. We plot the kT_e and L_X derived from the spectral fitting with the reflection model in Fig.9, which appear to still display the “ Λ ”-shaped correlation between them. We fit the correlation with the broken linear function Eq. (3), by replacing the X and Y with $\log L_X$ and $\log kT_e$ and excluding all the lower limits of kT_e . The best-fitting result is plotted as the dashed line. The correlation is broken at the luminosity $\log L_X = 37.20$, below which the slope is 0.62, and above which the correlation is -0.93 . The Spearman coefficients of the correlation for the data below and above this broken luminosity are 0.50 and -0.61 at the significances of 1.42σ and 3.16σ , respectively. This is qualitatively consistent with previous studies on BHXRBs (Yan et al. 2020).

5. CONCLUSIONS

In this work, we systematically study the evolution of the primary X-ray and the reflection component, for the *NuSTAR* sample of LMXBs in the hard state. The photon index Γ and

the reflection fraction R are well constrained. We find that R is positively correlated with Γ for the sample except for MAXI J1820+070. The positive $R - \Gamma$ correlation is in consistent with previous studies of LMXBs (Ueda et al. 1994; Zdziarski et al. 1999; Steiner et al. 2016) and AGNs (Diaz et al. 2020; Draghis et al. 2020; Connors et al. 2021). The Γ - R correlation could be explained in the scenarios of both the truncated disk and the outflowing X-ray source. Then we calculate the X-ray luminosity of the reflection model between 3 and 78 keV. It is interesting that there is a strong positive correlation between R and the X-ray luminosity for BHRBs in the hard state, which puts a constraint on the disk-corona coupling and the evolution. Moreover, We report “V”-shaped correlation between Γ and $\log L_x$ and “ Λ ”-shaped correlation between kT_e and $\log L_x$, which is in agreement with previous results. Combining the *NuSTAR* and *Insight*-HXMT results which obtained from (You et al. 2021), we find a negative $R - \Gamma$ correlation and a “ Λ ”-shaped correlation between Γ

and $\log L_x$ for MAXI J1820+070 in the bright hard state. The physical mechanism behind the particular behavior of MAXI J1820+070 is unknown. It challenges our knowledge of the accretion flow of black hole binary, and needs further exploration in the future.

1 We thank the referee for instructive suggestions and
 2 comments. This research has made use of data ob-
 3 tained by the High Energy Astrophysics Science Archive
 4 Research Center (HEASARC), which is an online ser-
 5 vice provided by NASA/GSFC. This work is supported
 6 by the National Key Research and Development Pro-
 7 gram of China (2021YFA0718500), the Natural Science
 8 Foundation of China (12273026, 11773050, 11833007,
 9 12073023, U1931203, 11903024, 11773055, U1838203,
 10 and U1938114), Youth Innovation Promotion Association of
 11 CAS (ID: 2020265), and the grant No. 2022CFB167.

REFERENCES

- Aramburu Sanchez, P., Neilsen, J., & Steiner, J. 2020, in American Astronomical Society Meeting Abstracts, Vol. 235, American Astronomical Society Meeting Abstracts #235, 369.14
- Arnaud, K. A. 1996, in ASP Conf. Ser., Vol. 101, Astronomical Data Analysis Software and Systems V, ed. G. H. Jacoby & J. Barnes, 17
- Atri, P., Miller-Jones, J. C. A., Bahramian, A., et al. 2020, MNRAS, 493, L81, doi: [10.1093/mnras/slao10](https://doi.org/10.1093/mnras/slao10)
- Bambi, C., Cárdenas-Avedaño, A., Dauser, T., García, J. A., & Nampalliwar, S. 2017, ApJ, 842, 76, doi: [10.3847/1538-4357/aa74c0](https://doi.org/10.3847/1538-4357/aa74c0)
- Beloborodov, A. M. 1999, The Astrophysical Journal, 510, L123, doi: [10.1086/311810](https://doi.org/10.1086/311810)
- Beri, A., Tetarenko, B. E., Bahramian, A., et al. 2019, MNRAS, 485, 3064, doi: [10.1093/mnras/stz616](https://doi.org/10.1093/mnras/stz616)
- Bharali, P., Chandra, S., Chauhan, J., et al. 2019, MNRAS, 487, 3150, doi: [10.1093/mnras/stz1492](https://doi.org/10.1093/mnras/stz1492)
- Brenneman, L. W., & Reynolds, C. S. 2006, ApJ, 652, 1028, doi: [10.1086/508146](https://doi.org/10.1086/508146)
- Buisson, D. J. K., Fabian, A. C., Barret, D., et al. 2019, MNRAS, 490, 1350, doi: [10.1093/mnras/stz2681](https://doi.org/10.1093/mnras/stz2681)
- Casares, J., Orosz, J. A., Zurita, C., et al. 2009, ApJS, 181, 238, doi: [10.1088/0067-0049/181/1/238](https://doi.org/10.1088/0067-0049/181/1/238)
- Chakraborty, S., Ratheesh, A., Bhattacharyya, S., et al. 2021, MNRAS, 508, 475, doi: [10.1093/mnras/stab2530](https://doi.org/10.1093/mnras/stab2530)
- Chand, S., Agrawal, V. K., Dewangan, G. C., Tripathi, P., & Thakur, P. 2020, ApJ, 893, 142, doi: [10.3847/1538-4357/ab829a](https://doi.org/10.3847/1538-4357/ab829a)
- Chauhan, J., Miller-Jones, J. C. A., Anderson, G. E., et al. 2019, MNRAS, 488, L129, doi: [10.1093/mnras/slz113](https://doi.org/10.1093/mnras/slz113)
- Chauhan, J., Miller-Jones, J. C. A., Raja, W., et al. 2021, MNRAS, 501, L60, doi: [10.1093/mnras/slao195](https://doi.org/10.1093/mnras/slao195)
- Connors, R., García, J., Tomsick, J., et al. 2021, arXiv e-prints, arXiv:2101.06343. <https://arxiv.org/abs/2101.06343>
- Curran, P. A. 2014, ArXiv e-prints, 1411, arXiv:1411.3816. <http://adsabs.harvard.edu/abs/2014arXiv1411.3816C>
- Dauser, T., García, J., Parker, M. L., Fabian, A. C., & Wilms, J. 2014, MNRAS, 444, L100, doi: [10.1093/mnras/slu125](https://doi.org/10.1093/mnras/slu125)
- Dauser, T., García, J., Walton, D. J., et al. 2016, A&A, 590, A76, doi: [10.1051/0004-6361/201628135](https://doi.org/10.1051/0004-6361/201628135)
- De Marco, B., Zdziarski, A. A., Ponti, G., et al. 2021, A&A, 654, A14, doi: [10.1051/0004-6361/202140567](https://doi.org/10.1051/0004-6361/202140567)
- De Marco, B., Ponti, G., Petrucci, P. O., et al. 2017, MNRAS, 471, 1475, doi: [10.1093/mnras/stx1649](https://doi.org/10.1093/mnras/stx1649)
- Diaz, Y., Arévalo, P., Hernández-García, L., et al. 2020, MNRAS, 496, 5399, doi: [10.1093/mnras/staa1762](https://doi.org/10.1093/mnras/staa1762)
- Done, C., Gierliński, M., & Kubota, A. 2007, A&A Rv, 15, 1, doi: [10.1007/s00159-007-0006-1](https://doi.org/10.1007/s00159-007-0006-1)
- Dong, Y., Liu, Z., Tuo, Y., et al. 2022, MNRAS, 514, 1422, doi: [10.1093/mnras/stac1466](https://doi.org/10.1093/mnras/stac1466)
- Draghis, P. A., Miller, J. M., Cackett, E. M., et al. 2020, ApJ, 900, 78, doi: [10.3847/1538-4357/aba2ec](https://doi.org/10.3847/1538-4357/aba2ec)
- El-Batal, A. M., Miller, J. M., Reynolds, M. T., et al. 2016, ApJL, 826, L12, doi: [10.3847/2041-8205/826/1/L12](https://doi.org/10.3847/2041-8205/826/1/L12)
- Esin, A. A., McClintock, J. E., & Narayan, R. 1997, ApJ, 489, 865, doi: [10.1086/304829](https://doi.org/10.1086/304829)
- Ezhikode, S. H., Dewangan, G. C., Misra, R., & Philip, N. S. 2020, MNRAS, 495, 3373, doi: [10.1093/mnras/staa1288](https://doi.org/10.1093/mnras/staa1288)
- Fabian, A. C., Lohfink, A., Kara, E., et al. 2015, MNRAS, 451, 4375, doi: [10.1093/mnras/stv1218](https://doi.org/10.1093/mnras/stv1218)

- Feng, Y., Zhao, X., Gou, L., et al. 2022, *Science China Physics, Mechanics, and Astronomy*, 65, 219512, doi: [10.1007/s11433-021-1790-7](https://doi.org/10.1007/s11433-021-1790-7)
- Foreman-Mackey, D., Hogg, D. W., Lang, D., & Goodman, J. 2013, *PASP*, 125, 306, doi: [10.1086/670067](https://doi.org/10.1086/670067)
- Fürst, F., Nowak, M. A., Tomsick, J. A., et al. 2015, *ApJ*, 808, 122, doi: [10.1088/0004-637X/808/2/122](https://doi.org/10.1088/0004-637X/808/2/122)
- Fürst, F., Tomsick, J. A., Yamaoka, K., et al. 2016, *ApJ*, 832, 115, doi: [10.3847/0004-637X/832/2/115](https://doi.org/10.3847/0004-637X/832/2/115)
- Gandhi, P., Rao, A., Johnson, M. A. C., Paice, J. A., & Maccarone, T. J. 2019, *MNRAS*, 485, 2642, doi: [10.1093/mnras/stz438](https://doi.org/10.1093/mnras/stz438)
- García, J., Dauser, T., Reynolds, C. S., et al. 2013, *ApJ*, 768, 146, doi: [10.1088/0004-637X/768/2/146](https://doi.org/10.1088/0004-637X/768/2/146)
- García, J., Dauser, T., Lohfink, A., et al. 2014, *ApJ*, 782, 76, doi: [10.1088/0004-637X/782/2/76](https://doi.org/10.1088/0004-637X/782/2/76)
- García, J. A., Dauser, T., Steiner, J. F., et al. 2015a, *ApJL*, 808, L37, doi: [10.1088/2041-8205/808/2/L37](https://doi.org/10.1088/2041-8205/808/2/L37)
- García, J. A., Steiner, J. F., McClintock, J. E., et al. 2015b, *ApJ*, 813, 84, doi: [10.1088/0004-637X/813/2/84](https://doi.org/10.1088/0004-637X/813/2/84)
- García, J. A., Tomsick, J. A., Sridhar, N., et al. 2019, *ApJ*, 885, 48, doi: [10.3847/1538-4357/ab384f](https://doi.org/10.3847/1538-4357/ab384f)
- George, I. M., & Fabian, A. C. 1991, *MNRAS*, 249, 352, doi: [10.1093/mnras/249.2.352](https://doi.org/10.1093/mnras/249.2.352)
- Gilfanov, M., Churazov, E., & Revnivtsev, M. 1999, *A&A*, 352, 182. <https://arxiv.org/abs/astro-ph/9910084>
- Harrison, F. A., Craig, W. W., Christensen, F. E., et al. 2013, *ApJ*, 770, 103, doi: [10.1088/0004-637X/770/2/103](https://doi.org/10.1088/0004-637X/770/2/103)
- Heida, M., Jonker, P. G., Torres, M. A. P., & Chiavassa, A. 2017, *ApJ*, 846, 132, doi: [10.3847/1538-4357/aa85df](https://doi.org/10.3847/1538-4357/aa85df)
- Ingram, A., van der Klis, M., Middleton, M., et al. 2016, *MNRAS*, 461, 1967, doi: [10.1093/mnras/stw1245](https://doi.org/10.1093/mnras/stw1245)
- Iyer, N., Nandi, A., & Mandal, S. 2015, *ApJ*, 807, 108, doi: [10.1088/0004-637X/807/1/108](https://doi.org/10.1088/0004-637X/807/1/108)
- Jana, A., Jaisawal, G. K., Naik, S., et al. 2021, *Research in Astronomy and Astrophysics*, 21, 125, doi: [10.1088/1674-4527/21/5/125](https://doi.org/10.1088/1674-4527/21/5/125)
- Jia, N., Zhao, X., Gou, L., et al. 2022, *MNRAS*, 511, 3125, doi: [10.1093/mnras/stac121](https://doi.org/10.1093/mnras/stac121)
- Jiang, J., Fabian, A. C., Wang, J., et al. 2019, *MNRAS*, 484, 1972, doi: [10.1093/mnras/stz095](https://doi.org/10.1093/mnras/stz095)
- Jiang, J., Fürst, F., Walton, D. J., Parker, M. L., & Fabian, A. C. 2020, *MNRAS*, 492, 1947, doi: [10.1093/mnras/staa017](https://doi.org/10.1093/mnras/staa017)
- Jiang, J., Buisson, D. J. K., Dauser, T., et al. 2022, *MNRAS*, 514, 1952, doi: [10.1093/mnras/stac1401](https://doi.org/10.1093/mnras/stac1401)
- Kang, J., Wang, J., & Kang, W. 2020, *ApJ*, 901, 111, doi: [10.3847/1538-4357/abadf5](https://doi.org/10.3847/1538-4357/abadf5)
- Kara, E., Steiner, J. F., Fabian, A. C., et al. 2019, *Nature*, 565, 198, doi: [10.1038/s41586-018-0803-x](https://doi.org/10.1038/s41586-018-0803-x)
- Kawamura, T., Axelsson, M., Done, C., & Takahashi, T. 2022, *MNRAS*, 511, 536, doi: [10.1093/mnras/stac045](https://doi.org/10.1093/mnras/stac045)
- Kelly, B. C. 2007, *ApJ*, 665, 1489, doi: [10.1086/519947](https://doi.org/10.1086/519947)
- Klepczarek, Ł., Niedźwiecki, A., & Szanecki, M. 2023, *MNRAS*, 519, L79, doi: [10.1093/mnras/slac156](https://doi.org/10.1093/mnras/slac156)
- Koljonen, K. I. I., & Tomsick, J. A. 2020, *A&A*, 639, A13, doi: [10.1051/0004-6361/202037882](https://doi.org/10.1051/0004-6361/202037882)
- Kubota, A., & Makishima, K. 2004, *ApJ*, 601, 428, doi: [10.1086/380433](https://doi.org/10.1086/380433)
- Kubota, A., Tanaka, Y., Makishima, K., et al. 1998, *PASJ*, 50, 667, doi: [10.1093/pasj/50.6.667](https://doi.org/10.1093/pasj/50.6.667)
- Liu, B. F., & Qiao, E. 2022, *iSci*, 25, 103544, doi: [10.1016/j.isci.2021.103544](https://doi.org/10.1016/j.isci.2021.103544)
- Madsen, K. K., Grefenstette, B. W., Pike, S., et al. 2020, arXiv e-prints, arXiv:2005.00569. <https://arxiv.org/abs/2005.00569>
- Mahmoud, R. D., & Done, C. 2018, *MNRAS*, 480, 4040, doi: [10.1093/mnras/sty2133](https://doi.org/10.1093/mnras/sty2133)
- Marino, A., Barnier, S., Petrucci, P. O., et al. 2021, *A&A*, 656, A63, doi: [10.1051/0004-6361/202141146](https://doi.org/10.1051/0004-6361/202141146)
- Miller, J. M., Parker, M. L., Fuerst, F., et al. 2013, *ApJL*, 775, L45, doi: [10.1088/2041-8205/775/2/L45](https://doi.org/10.1088/2041-8205/775/2/L45)
- Miller, J. M., Tomsick, J. A., Bachetti, M., et al. 2015, *The Astrophysical Journal*, 799, L6, doi: [10.1088/2041-8205/799/1/L6](https://doi.org/10.1088/2041-8205/799/1/L6)
- Muñoz-Darias, T., Coriat, M., Plant, D. S., et al. 2013, *MNRAS*, 432, 1330, doi: [10.1093/mnras/stt546](https://doi.org/10.1093/mnras/stt546)
- Neustroev, V. V., Veledina, A., Poutanen, J., et al. 2014, *MNRAS*, 445, 2424, doi: [10.1093/mnras/stu1924](https://doi.org/10.1093/mnras/stu1924)
- Panagiotou, C., & Walter, R. 2020, *A&A*, 640, A31, doi: [10.1051/0004-6361/201937390](https://doi.org/10.1051/0004-6361/201937390)
- Plant, D. S., Fender, R. P., Ponti, G., Muñoz-Darias, T., & Coriat, M. 2014, *MNRAS*, 442, 1767, doi: [10.1093/mnras/stu867](https://doi.org/10.1093/mnras/stu867)
- , 2015, *A&A*, 573, A120, doi: [10.1051/0004-6361/201423925](https://doi.org/10.1051/0004-6361/201423925)
- Ponti, G., Fender, R. P., Begelman, M. C., et al. 2012, *MNRAS*, 422, L11, doi: [10.1111/j.1745-3933.2012.01224.x](https://doi.org/10.1111/j.1745-3933.2012.01224.x)
- Poutanen, J., Veledina, A., & Zdziarski, A. A. 2018, *A&A*, 614, A79, doi: [10.1051/0004-6361/201732345](https://doi.org/10.1051/0004-6361/201732345)
- Poutanen, J., Veledina, A., Berdyugin, A. V., et al. 2022, *Science*, 375, 874, doi: [10.1126/science.abl4679](https://doi.org/10.1126/science.abl4679)
- Prabhakar, G., Mandal, S., Athulya, M. P., & Nandi, A. 2022, *MNRAS*, 514, 6102, doi: [10.1093/mnras/stac1176](https://doi.org/10.1093/mnras/stac1176)
- Qiao, E., & Liu, B. F. 2012, *ApJ*, 744, 145, doi: [10.1088/0004-637X/744/2/145](https://doi.org/10.1088/0004-637X/744/2/145)
- , 2017, *MNRAS*, 467, 898, doi: [10.1093/mnras/stx121](https://doi.org/10.1093/mnras/stx121)
- Reid, M. J., McClintock, J. E., Steiner, J. F., et al. 2014, *ApJ*, 796, 2, doi: [10.1088/0004-637X/796/1/2](https://doi.org/10.1088/0004-637X/796/1/2)
- Revnivtsev, M., Gilfanov, M., & Churazov, E. 2001, *A&A*, 380, 520, doi: [10.1051/0004-6361:20011413](https://doi.org/10.1051/0004-6361:20011413)
- Ross, R. R., & Fabian, A. C. 2005, *MNRAS*, 358, 211, doi: [10.1111/j.1365-2966.2005.08797.x](https://doi.org/10.1111/j.1365-2966.2005.08797.x)
- Rout, S. K., Vadawale, S., Garcia, J., & Connors, R. 2022, arXiv e-prints, arXiv:2212.05293. <https://arxiv.org/abs/2212.05293>

- Saikia, P., Russell, D. M., Baglio, M. C., et al. 2022, *ApJ*, 932, 38, doi: [10.3847/1538-4357/ac6ce1](https://doi.org/10.3847/1538-4357/ac6ce1)
- Shaw, A. W., Charles, P. A., Casares, J., & Hernández Santisteban, J. V. 2016a, *MNRAS*, 463, 1314, doi: [10.1093/mnras/stw2092](https://doi.org/10.1093/mnras/stw2092)
- Shaw, A. W., Gandhi, P., Altamirano, D., et al. 2016b, *MNRAS*, 458, 1636, doi: [10.1093/mnras/stw417](https://doi.org/10.1093/mnras/stw417)
- Shreeram, S., & Ingram, A. 2020, *MNRAS*, 492, 405, doi: [10.1093/mnras/stz3455](https://doi.org/10.1093/mnras/stz3455)
- Sridhar, N., García, J. A., Steiner, J. F., et al. 2020, *ApJ*, 890, 53, doi: [10.3847/1538-4357/ab64f5](https://doi.org/10.3847/1538-4357/ab64f5)
- Steiner, J. F., McClintock, J. E., & Reid, M. J. 2012, *ApJL*, 745, L7, doi: [10.1088/2041-8205/745/1/L7](https://doi.org/10.1088/2041-8205/745/1/L7)
- Steiner, J. F., Remillard, R. A., García, J. A., & McClintock, J. E. 2016, *ApJL*, 829, L22, doi: [10.3847/2041-8205/829/2/L22](https://doi.org/10.3847/2041-8205/829/2/L22)
- Stiele, H., & Kong, A. K. H. 2021, *ApJ*, 914, 93, doi: [10.3847/1538-4357/abfaa5](https://doi.org/10.3847/1538-4357/abfaa5)
- Torres, M. A. P., Casares, J., Jiménez-Ibarra, F., et al. 2020, *ApJL*, 893, L37, doi: [10.3847/2041-8213/ab863a](https://doi.org/10.3847/2041-8213/ab863a)
- Tripathi, A., Zhang, Y., Abdikamalov, A. B., et al. 2021, *ApJ*, 913, 79, doi: [10.3847/1538-4357/abf6cd](https://doi.org/10.3847/1538-4357/abf6cd)
- Ueda, Y., Ebisawa, K., & Done, C. 1994, *PASJ*, 46, 107
- Uttley, P., Gendreau, K., Markwardt, C., et al. 2018, *The Astronomer's Telegram*, 11423, 1
- Walton, D. J., Mooley, K., King, A. L., et al. 2017, *ApJ*, 839, 110, doi: [10.3847/1538-4357/aa67e8](https://doi.org/10.3847/1538-4357/aa67e8)
- Wang, J., Kara, E., Steiner, J. F., et al. 2020a, *ApJ*, 899, 44, doi: [10.3847/1538-4357/ab9ec3](https://doi.org/10.3847/1538-4357/ab9ec3)
- Wang, P. J., Kong, L. D., Chen, Y. P., et al. 2022, *MNRAS*, 512, 4541, doi: [10.1093/mnras/stac773](https://doi.org/10.1093/mnras/stac773)
- Wang, Y., Ji, L., Zhang, S. N., et al. 2020b, *ApJ*, 896, 33, doi: [10.3847/1538-4357/ab8db4](https://doi.org/10.3847/1538-4357/ab8db4)
- Wang-Ji, J., García, J. A., Steiner, J. F., et al. 2018, *ApJ*, 855, 61, doi: [10.3847/1538-4357/aaa974](https://doi.org/10.3847/1538-4357/aaa974)
- Wilms, J., Allen, A., & McCray, R. 2000, *ApJ*, 542, 914, doi: [10.1086/317016](https://doi.org/10.1086/317016)
- Wu, Q., & Gu, M. 2008, *ApJ*, 682, 212, doi: [10.1086/588187](https://doi.org/10.1086/588187)
- Xu, Y., Nampalliwar, S., Abdikamalov, A. B., et al. 2018a, *ApJ*, 865, 134, doi: [10.3847/1538-4357/aadb9d](https://doi.org/10.3847/1538-4357/aadb9d)
- Xu, Y., García, J. A., Fürst, F., et al. 2017, *ApJ*, 851, 103, doi: [10.3847/1538-4357/aa9ab4](https://doi.org/10.3847/1538-4357/aa9ab4)
- Xu, Y., Harrison, F. A., García, J. A., et al. 2018b, *ApJL*, 852, L34, doi: [10.3847/2041-8213/aaa4b2](https://doi.org/10.3847/2041-8213/aaa4b2)
- Yamaoka, K., Uzawa, M., Arai, M., Yamazaki, T., & Yoshida, A. 2005, *Chinese Journal of Astronomy and Astrophysics Supplement*, 5, 273
- Yan, Z., Xie, F.-G., & Zhang, W. 2020, *ApJL*, 889, L18, doi: [10.3847/2041-8213/ab665e](https://doi.org/10.3847/2041-8213/ab665e)
- Yan, Z., & Yu, W. 2017, *MNRAS*, 470, 4298, doi: [10.1093/mnras/stx1562](https://doi.org/10.1093/mnras/stx1562)
- Yang, Q.-X., Xie, F.-G., Yuan, F., et al. 2015, *MNRAS*, 447, 1692, doi: [10.1093/mnras/stu2571](https://doi.org/10.1093/mnras/stu2571)
- You, B., Cao, X., & Yuan, Y.-F. 2012, *ApJ*, 761, 109, doi: [10.1088/0004-637X/761/2/109](https://doi.org/10.1088/0004-637X/761/2/109)
- You, B., Tuo, Y., Li, C., et al. 2021, *Nature Communications*, 12, 1025, doi: [10.1038/s41467-021-21169-5](https://doi.org/10.1038/s41467-021-21169-5)
- Yuan, F., & Narayan, R. 2014, *ARA&A*, 52, 529, doi: [10.1146/annurev-astro-082812-141003](https://doi.org/10.1146/annurev-astro-082812-141003)
- Zdziarski, A. A., Dziełak, M. A., De Marco, B., Szanecki, M., & Niedźwiecki, A. 2021a, *ApJL*, 909, L9, doi: [10.3847/2041-8213/abe7ef](https://doi.org/10.3847/2041-8213/abe7ef)
- Zdziarski, A. A., Johnson, W. N., & Magdziarz, P. 1996, *MNRAS*, 283, 193, doi: [10.1093/mnras/283.1.193](https://doi.org/10.1093/mnras/283.1.193)
- Zdziarski, A. A., Lubiński, P., & Smith, D. A. 1999, *MNRAS*, 303, L11, doi: [10.1046/j.1365-8711.1999.02343.x](https://doi.org/10.1046/j.1365-8711.1999.02343.x)
- Zdziarski, A. A., You, B., & Szanecki, M. 2022a, *ApJL*, 939, L2, doi: [10.3847/2041-8213/ac9474](https://doi.org/10.3847/2041-8213/ac9474)
- Zdziarski, A. A., You, B., Szanecki, M., Li, X.-B., & Ge, M. 2022b, *ApJ*, 928, 11, doi: [10.3847/1538-4357/ac54a7](https://doi.org/10.3847/1538-4357/ac54a7)
- Zdziarski, A. A., Ziółkowski, J., & Mikołajewska, J. 2019, *MNRAS*, 488, 1026, doi: [10.1093/mnras/stz1787](https://doi.org/10.1093/mnras/stz1787)
- Zdziarski, A. A., Jourdain, E., Lubiński, P., et al. 2021b, *ApJL*, 914, L5, doi: [10.3847/2041-8213/ac0147](https://doi.org/10.3847/2041-8213/ac0147)
- Zhang, Y., Abdikamalov, A. B., Ayzenberg, D., et al. 2019a, *ApJ*, 875, 41, doi: [10.3847/1538-4357/ab0e79](https://doi.org/10.3847/1538-4357/ab0e79)
- Zhang, Y., Abdikamalov, A. B., Ayzenberg, D., Bambi, C., & Nampalliwar, S. 2019b, *ApJ*, 884, 147, doi: [10.3847/1538-4357/ab4271](https://doi.org/10.3847/1538-4357/ab4271)

Table 2. *NuSTAR* observation Details

Source	ObsID	Detector	MJD	Exp.	Counts (s ⁻¹)	HR
GRS 1716-249	80201034006	FPMA	57758.50	6046.56	113.90 ± 0.14	0.47
		FPMB	57758.50	6134.49	108.20 ± 0.13	0.46
	80201034007	FPMA	57781.32	42465.19	129.50 ± 0.06	0.48
		FPMB	57781.32	43515.15	119.30 ± 0.05	0.47
	90202055002	FPMA	57850.61	17897.52	125.40 ± 0.08	0.40
		FPMB	57850.61	18259.78	115.70 ± 0.08	0.39
	90202055004	FPMA	57853.70	15797.47	121.70 ± 0.09	0.38
		FPMB	57853.70	16100.69	112.70 ± 0.08	0.36
GRS 1739-278	80101050002	FPMA	57280.89	41241.62	0.35 ± 0.00	0.50
		FPMB	57280.89	40965.48	0.38 ± 0.00	0.43
	80102101002	FPMA	57660.89	26310.03	3.14 ± 0.01	0.49
		FPMB	57660.89	26102.79	3.00 ± 0.01	0.47
	80102101004	FPMA	57680.63	25897.14	0.88 ± 0.01	0.49
		FPMB	57680.63	25703.41	0.88 ± 0.01	0.46
	80102101005	FPMA	57692.85	27021.16	1.93 ± 0.01	0.49
		FPMB	57692.85	26903.39	1.78 ± 0.01	0.47
GRS 1915+105	10002004001	FPMA	56111.06	14696.17	195.00 ± 0.12	0.32
		FPMB	56111.06	15114.49	181.70 ± 0.11	0.32
	80401312002	FPMA	58277.51	26167.74	82.96 ± 0.06	0.33
		FPMB	58277.51	26396.31	76.44 ± 0.05	0.32
	90202045002	FPMA	57806.17	13903.36	169.20 ± 0.11	0.31
		FPMB	57806.17	14093.44	158.60 ± 0.11	0.30
GS 1354-64	90101006002	FPMA	57186.30	24021.18	6.94 ± 0.02	0.60
		FPMB	57186.30	23694.70	6.37 ± 0.02	0.58
	90101006004	FPMA	57214.59	28797.52	48.24 ± 0.04	0.52
		FPMB	57214.59	28624.73	44.72 ± 0.04	0.50
	90101006006	FPMA	57240.31	34965.82	54.92 ± 0.04	0.47
		FPMB	57240.31	35030.46	51.89 ± 0.04	0.46
GX 339-4	80001013002	FPMA	56516.01	35090.43	10.41 ± 0.02	0.53
		FPMB	56516.01	35098.32	10.15 ± 0.02	0.52
	80001013004	FPMA	56520.75	20794.25	17.41 ± 0.03	0.53
		FPMB	56520.75	20834.18	16.42 ± 0.03	0.52
	80001013006	FPMA	56528.54	23152.06	27.74 ± 0.03	0.52
		FPMB	56528.54	23244.36	26.10 ± 0.03	0.51
	80001013008	FPMA	56538.44	43189.25	36.39 ± 0.03	0.51
		FPMB	56538.44	43438.82	34.54 ± 0.03	0.50
	80001013010	FPMA	56582.00	97569.81	6.16 ± 0.01	0.50
		FPMB	56582.00	97944.22	5.87 ± 0.01	0.49
	80001015001	FPMA	57035.24	10377.22	103.70 ± 0.10	0.38
		FPMB	57035.24	10549.82	96.38 ± 0.10	0.37
	80102011002	FPMA	57262.56	18249.12	18.76 ± 0.03	0.39
		FPMB	57262.56	17658.19	17.54 ± 0.03	0.38
	80102011004	FPMA	57267.53	17370.83	16.44 ± 0.03	0.45
		FPMB	57267.53	17202.23	15.33 ± 0.03	0.44
	80102011006	FPMA	57272.63	16239.13	13.87 ± 0.03	0.47
		FPMB	57272.63	16091.85	13.03 ± 0.03	0.45
	80102011010	FPMA	57282.43	35689.01	7.70 ± 0.01	0.49

Table 2. continued.

Source	ObsID	Detector	MJD	Exp.	Counts (s ⁻¹)	HR
		FPMB	57282.43	35563.32	7.27 ± 0.01	0.47
	80102011012	FPMA	57295.06	41332.23	4.15 ± 0.01	0.48
		FPMB	57295.06	41322.83	3.87 ± 0.01	0.46
	80302304002	FPMA	58028.15	20523.68	2.38 ± 0.01	0.48
		FPMB	58028.15	20767.70	2.23 ± 0.01	0.46
	80302304004	FPMA	58051.58	17046.56	21.97 ± 0.04	0.51
		FPMB	58051.58	16956.34	20.58 ± 0.04	0.50
	80302304005	FPMA	58059.90	18515.38	19.72 ± 0.03	0.51
		FPMB	58059.90	18534.54	18.39 ± 0.03	0.49
	80502325008	FPMA	58959.06	22397.06	10.33 ± 0.02	0.44
		FPMB	58959.06	22166.46	9.57 ± 0.02	0.43
	90401369004	FPMA	58488.63	3621.66	13.05 ± 0.06	0.52
		FPMB	58488.63	3616.51	12.04 ± 0.06	0.50
H1743-322	80001044002	FPMA	56918.66	50252.45	26.22 ± 0.02	0.57
		FPMB	56918.66	50387.07	25.39 ± 0.02	0.55
	80001044004	FPMA	56923.77	61278.07	34.86 ± 0.02	0.54
		FPMB	56923.77	61339.79	33.88 ± 0.02	0.53
	80001044006	FPMA	56939.78	25666.98	31.02 ± 0.03	0.55
		FPMB	56939.78	25721.70	29.17 ± 0.03	0.53
	80002040002	FPMA	57206.13	27418.52	18.02 ± 0.03	0.56
		FPMB	57206.13	27603.63	16.53 ± 0.02	0.54
	80202012002	FPMA	57460.07	65869.27	38.61 ± 0.02	0.44
		FPMB	57460.07	66283.17	36.43 ± 0.02	0.43
	80202012004	FPMA	57462.29	64870.79	37.00 ± 0.02	0.44
		FPMB	57462.29	65040.59	34.68 ± 0.02	0.43
	80202012006	FPMA	58387.37	65702.67	20.10 ± 0.02	0.54
		FPMB	58387.37	65610.73	18.99 ± 0.02	0.53
	90401335002	FPMA	58380.12	38443.65	32.36 ± 0.03	0.52
		FPMB	58380.12	38425.23	30.52 ± 0.03	0.51
IGR J17091-3624	80001041002	FPMA	57454.09	43297.76	15.80 ± 0.02	0.52
		FPMB	57454.09	42957.81	14.75 ± 0.02	0.51
	80202014002	FPMA	57459.60	20239.92	20.64 ± 0.03	0.50
		FPMB	57459.60	20278.74	19.23 ± 0.03	0.48
	80202014004	FPMA	57461.81	20700.15	22.79 ± 0.03	0.48
		FPMB	57461.81	20515.16	21.24 ± 0.03	0.46
MAXI J1348-630	80402315002	FPMA	58515.13	3038.04	1043.00 ± 0.59	0.43
		FPMB	58515.13	3208.37	906.00 ± 0.53	0.42
	80402315004	FPMA	58515.60	736.34	1048.00 ± 1.20	0.42
		FPMB	58515.60	778.54	911.50 ± 1.09	0.42
	80502304002	FPMA	58655.40	13783.86	186.80 ± 0.12	0.45
		FPMB	58655.40	14172.58	172.20 ± 0.11	0.44
	80502304004	FPMA	58660.50	15367.24	161.90 ± 0.10	0.47
		FPMB	58660.50	15773.25	149.50 ± 0.10	0.46
	80502304006	FPMA	58672.38	17181.65	107.60 ± 0.08	0.48
		FPMB	58672.38	17460.58	100.00 ± 0.08	0.47
MAXI J1535-571	90301013002	FPMA	58003.79	10142.25	609.40 ± 0.25	0.41
		FPMB	58003.79	10670.31	549.40 ± 0.23	0.40

Table 2. continued.

Source	ObsID	Detector	MJD	Exp.	Counts (s ⁻¹)	HR	
MAXI J1813-095	80402303002	FPMA	58177.50	20546.62	16.18 ± 0.03	0.50	
		FPMB	58177.50	20002.84	15.16 ± 0.03	0.49	
	80402303004	FPMA	58183.60	20433.92	13.43 ± 0.03	0.49	
		FPMB	58183.60	20346.84	12.69 ± 0.03	0.49	
	80402303006	FPMA	58202.73	23238.40	14.52 ± 0.03	0.46	
		FPMB	58202.73	23099.06	13.66 ± 0.02	0.45	
MAXI J1820+070	90401309002	FPMA	58191.94	11769.40	178.90 ± 0.12	0.56	
		FPMB	58191.94	11980.90	169.90 ± 0.12	0.55	
	90401309004	FPMA	58198.04	2760.78	735.20 ± 0.52	0.49	
		FPMB	58198.04	2876.89	663.50 ± 0.48	0.48	
	90401309006	FPMA	58198.30	4539.90	761.20 ± 0.41	0.49	
		FPMB	58198.30	4762.39	681.20 ± 0.38	0.48	
	90401309008	FPMA	58201.53	3046.06	776.90 ± 0.51	0.48	
		FPMB	58201.53	3214.09	689.60 ± 0.47	0.47	
	90401309010	FPMA	58201.86	2660.36	782.70 ± 0.54	0.48	
		FPMB	58201.86	2801.44	697.00 ± 0.50	0.47	
	90401309012	FPMA	58212.20	12334.25	695.40 ± 0.24	0.47	
		FPMB	58212.20	12964.31	624.30 ± 0.22	0.46	
	90401309013	FPMA	58224.95	1834.38	672.60 ± 0.61	0.46	
		FPMB	58224.95	1934.06	597.70 ± 0.59	0.45	
	90401309014	FPMA	58225.29	9208.80	677.90 ± 0.27	0.46	
		FPMB	58225.29	9708.55	603.80 ± 0.25	0.45	
	90401309016	FPMA	58241.80	13792.23	572.90 ± 0.21	0.43	
		FPMB	58241.80	14431.53	514.60 ± 0.21	0.42	
	90401309018	FPMA	58255.16	2733.45	504.50 ± 0.48	0.42	
		FPMB	58255.16	2879.63	457.10 ± 0.40	0.41	
	90401309019	FPMA	58255.63	9444.10	503.40 ± 0.25	0.42	
		FPMB	58255.63	9938.34	455.80 ± 0.21	0.41	
	90401309021	FPMA	58297.17	21867.83	301.10 ± 0.12	0.43	
		FPMB	58297.17	22852.97	272.20 ± 0.11	0.42	
	90401309033	FPMA	58388.92	24892.60	124.20 ± 0.07	0.31	
		FPMB	58388.92	25342.94	116.50 ± 0.07	0.31	
	90401309035	FPMA	58397.30	18569.88	53.27 ± 0.05	0.44	
		FPMB	58397.30	18640.73	50.71 ± 0.05	0.44	
	90401309037	FPMA	58404.95	37682.99	14.04 ± 0.02	0.42	
		FPMB	58404.95	37608.34	13.18 ± 0.02	0.41	
	90401324002	FPMA	58259.25	6570.79	486.70 ± 0.27	0.42	
		FPMB	58259.25	6931.40	438.00 ± 0.25	0.41	
	90501311002	FPMA	58567.83	28666.65	13.82 ± 0.02	0.43	
		FPMB	58567.83	28590.56	12.92 ± 0.02	0.42	
	90501337002	FPMA	58721.31	44577.57	14.25 ± 0.02	0.43	
		FPMB	58721.31	44311.46	13.28 ± 0.02	0.43	
	Swift J1753.5-0127	30001148002	FPMA	56913.42	40434.75	12.32 ± 0.02	0.42
			FPMB	56913.42	40476.89	11.69 ± 0.02	0.41

Table 3. Best-fitting Results of the *NuSTAR* sample

ObsID	T_{in} (keV)	N_{disk}	q	i (deg.)	R_{in} (R_{ISCO})	Γ	$\log\xi$	A_{Fe}	kT_{e} (keV)	R_{f}	N_{rel} ($\times 10^{-4}$)	N_{Hl} ($\times 10^{-4}$)	χ^2/ν
GRS 1716-249 ^(a)													
80201034006	$0.45^{+0.01}_{-0.01}$	$2609.8^{+404.3}_{-397.3}$	$2.5^{+0.3}_{-0.3}$	$9.8^{+0.9}_{-1.6}$	$4.6^{+0.8}_{-1.0}$	$1.584^{+0.007}_{-0.006}$	$3.91^{+0.07}_{-0.10}$	$2.8^{+0.2}_{-0.3}$	$48.5^{+4.9}_{-4.7}$	$0.16^{+0.02}_{-0.02}$	$267.4^{+10.2}_{-10.3}$	-	-
80201034007	$0.46^{+0.01}_{-0.01}$	$2927.5^{+416.7}_{-551.2}$	10.0^*	...	$7.9^{+0.5}_{-0.7}$	$1.515^{+0.005}_{-0.006}$	$4.06^{+0.02}_{-0.03}$...	$339.4^{+36.1}_{-35.7}$	$0.39^{+0.04}_{-0.03}$	$292.1^{+10.8}_{-8.2}$	-	$\frac{5696.9}{5600}$
90202055002	$0.49^{+0.01}_{-0.01}$	$2050.2^{+244.1}_{-242.9}$	$3.3^{+0.4}_{-0.6}$...	$8.3^{+1.4}_{-1.1}$	$1.663^{+0.007}_{-0.007}$	$4.11^{+0.03}_{-0.03}$...	400^*	$0.48^{+0.04}_{-0.05}$	$191.9^{+9.8}_{-8.2}$	-	-
90202055004	$0.51^{+0.01}_{-0.01}$	$1634.4^{+229.4}_{-149.5}$	10.0^*	...	$63.7^{+25.3}_{-16.0}$	$1.771^{+0.006}_{-0.007}$	$3.94^{+0.07}_{-0.06}$...	$87.7^{+17.7}_{-14.3}$	$0.21^{+0.04}_{-0.03}$	$217.2^{+7.7}_{-12.2}$	-	-
GRS 1739-278 ^(b)													
80101050002	-	-	-	-	-	$1.824^{+0.035}_{-0.034}$	-	-	$11.3^{+4.0}_{-2.5}$	-	$44.2^{+3.8}_{-3.5}$	-	-
80102101002	-	-	-	-	-	$1.68^{+0.013}_{-0.008}$	-	-	> 34.4	-	$265.5^{+6.9}_{-5.4}$	-	$\frac{2733.27}{2845}$
80102101004	-	-	-	-	-	$1.699^{+0.036}_{-0.019}$	-	-	> 30.4	-	$82.6^{+4.7}_{-3.7}$	-	-
80102101005	-	-	-	-	-	$1.670^{+0.016}_{-0.014}$	-	-	> 175.6	-	$166.8^{+5.2}_{-6.3}$	-	-
GRS 1915+105 ^(c)													
10002004001	$0.35^{+0.01}_{-0.00}$	$184770.9^{+24440.3}_{-32299.6}$	$2.2^{+0.1}_{-0.1}$	60^{\dagger}	$2.8^{+0.5}_{-0.2}$	$1.942^{+0.003}_{-0.003}$	4.50^*	$3.7^{+0.1}_{-0.1}$	$16.6^{+0.3}_{-0.3}$	$2.54^{+0.12}_{-0.11}$	$141.1^{+5.8}_{-4.3}$	$30.9^{+3.9}_{-3.7}$	-
80401312002	$0.48^{+0.01}_{-0.01}$	$6891.3^{+1061.8}_{-1013.5}$	$3.8^{+0.7}_{-0.4}$...	$8.4^{+1.2}_{-1.2}$	$1.952^{+0.006}_{-0.005}$	$4.01^{+0.03}_{-0.02}$...	$65.7^{+9.2}_{-7.7}$	$1.27^{+0.11}_{-0.08}$	$108.0^{+4.9}_{-4.6}$	$15.0^{+1.9}_{-2.3}$	$\frac{3938.3}{3602}$
90202045002	$0.40^{+0.01}_{-0.01}$	$53310.0^{+9836.9}_{-8274.3}$	$2.4^{+0.2}_{-0.1}$...	$3.3^{+1.1}_{-1.0}$	$1.970^{+0.003}_{-0.003}$	$4.40^{+0.02}_{-0.02}$...	$35.2^{+1.7}_{-1.6}$	$2.76^{+0.09}_{-0.06}$	$127.6^{+2.4}_{-3.1}$	$19.7^{+3.3}_{-2.6}$	-
GS 1354-64 ^(d)													
90101006002	-	-	$4.4^{+3.2}_{-2.2}$	$29.0^{+3.7}_{-3.3}$	$56.9^{+48.4}_{-25.8}$	$1.505^{+0.010}_{-0.011}$	$3.03^{+0.24}_{-0.19}$	0.5^*	$46.1^{+11.9}_{-8.4}$	$0.14^{+0.03}_{-0.04}$	$20.3^{+1.8}_{-1.2}$	-	-
90101006004	-	-	$2.7^{+1.2}_{-0.4}$...	$9.8^{+11.9}_{-8.3}$	$1.623^{+0.007}_{-0.006}$	$2.97^{+0.07}_{-0.06}$...	$18.7^{+1.0}_{-0.5}$	$0.24^{+0.08}_{-0.03}$	$83.6^{+1.4}_{-1.8}$	-	$\frac{3871.9}{3470}$
90101006006	-	-	$4.6^{+2.9}_{-1.5}$...	$44.1^{+37.4}_{-16.3}$	$1.663^{+0.003}_{-0.003}$	$3.48^{+0.06}_{-0.07}$...	$19.1^{+0.6}_{-0.6}$	$0.25^{+0.04}_{-0.04}$	$82.4^{+2.6}_{-2.7}$	-	-
GX 339-4 ^(e)													
80001013002	-	-	$2.48^{+0.05}_{-0.04}$	40^{\dagger}	$1.18^{+0.00}_{-0.00}$	$1.585^{+0.002}_{-0.002}$	$1.93^{+0.03}_{-0.03}$	$5.3^{+0.1}_{-0.1}$	$240.8^{+2.1}_{-3.1}$	$0.255^{+0.009}_{-0.005}$	$36.6^{+0.3}_{-0.5}$	-	-
80001013004	-	-	$2.85^{+0.05}_{-0.05}$...	1.0^*	$1.588^{+0.002}_{-0.003}$	$3.01^{+0.04}_{-0.05}$...	$316.9^{+4.9}_{-4.5}$	$0.275^{+0.008}_{-0.006}$	$59.0^{+1.1}_{-0.9}$	-	-
80001013006	-	-	$6.25^{+0.04}_{-0.05}$...	$4.13^{+0.13}_{-0.13}$	$1.591^{+0.004}_{-0.004}$	$2.97^{+0.07}_{-0.03}$...	400^*	$0.272^{+0.005}_{-0.005}$	$94.9^{+0.6}_{-1.3}$	-	-
80001013008	-	-	$2.83^{+0.06}_{-0.07}$...	1.0^*	$1.579^{+0.006}_{-0.004}$	$3.09^{+0.03}_{-0.07}$...	400^*	$0.310^{+0.005}_{-0.005}$	$125.0^{+1.7}_{-0.8}$	-	-
80001013010	-	-	$2.04^{+0.08}_{-0.10}$...	$31.43^{+1.19}_{-0.65}$	$1.598^{+0.004}_{-0.003}$	$1.73^{+0.02}_{-0.03}$...	$67.9^{+2.0}_{-1.4}$	$0.127^{+0.001}_{-0.002}$	$18.2^{+0.3}_{-0.1}$	-	-
80001015001	-	-	$2.87^{+0.03}_{-0.03}$...	1.0^*	$1.752^{+0.004}_{-0.003}$	$3.44^{+0.01}_{-0.01}$...	$48.8^{+1.0}_{-2.2}$	$0.311^{+0.004}_{-0.006}$	$198.7^{+1.0}_{-2.4}$	-	-
80102011002	-	-	$7.46^{+0.05}_{-0.10}$...	$3.47^{+0.06}_{-0.04}$	$1.748^{+0.003}_{-0.003}$	$3.51^{+0.02}_{-0.04}$...	400^*	$0.395^{+0.015}_{-0.007}$	$38.3^{+0.6}_{-0.4}$	-	-
80102011004	-	-	$5.07^{+0.04}_{-0.07}$...	$2.88^{+0.05}_{-0.06}$	$1.669^{+0.002}_{-0.006}$	$3.30^{+0.05}_{-0.06}$...	400^*	$0.254^{+0.004}_{-0.005}$	$43.2^{+0.4}_{-0.3}$	-	-
80102011006	-	-	10.0^*	...	$3.63^{+0.05}_{-0.07}$	$1.656^{+0.004}_{-0.004}$	$2.99^{+0.02}_{-0.02}$...	400^*	$0.239^{+0.003}_{-0.012}$	$41.1^{+0.5}_{-0.9}$	-	-
80102011010	-	-	$2.33^{+0.05}_{-0.05}$...	$1.34^{+0.00}_{-0.01}$	$1.640^{+0.002}_{-0.003}$	$3.00^{+0.07}_{-0.02}$...	400^*	$0.165^{+0.003}_{-0.002}$	$24.7^{+0.6}_{-0.2}$	-	-
80102011012	-	-	$2.66^{+0.04}_{-0.03}$...	$11.65^{+0.37}_{-0.30}$	$1.657^{+0.002}_{-0.002}$	$2.62^{+0.03}_{-0.03}$...	$187.2^{+9.4}_{-2.9}$	$0.169^{+0.003}_{-0.005}$	$11.9^{+0.2}_{-0.1}$	-	-
80302304002	-	-	$1.73^{+0.05}_{-0.04}$...	1.0^*	$1.648^{+0.002}_{-0.003}$	$2.93^{+0.05}_{-0.02}$...	$47.6^{+1.0}_{-1.0}$	$0.165^{+0.004}_{-0.003}$	$5.7^{+0.1}_{-0.1}$	-	-
80302304004	-	-	10.0^*	...	$3.33^{+0.04}_{-0.05}$	$1.564^{+0.003}_{-0.004}$	$3.16^{+0.02}_{-0.04}$...	400^*	$0.318^{+0.005}_{-0.009}$	$81.0^{+2.4}_{-0.7}$	-	-
80302304005	-	-	10.0^*	...	$2.95^{+0.17}_{-0.08}$	$1.612^{+0.002}_{-0.009}$	$3.02^{+0.02}_{-0.01}$...	400^*	$0.286^{+0.006}_{-0.004}$	$66.4^{+0.5}_{-0.5}$	-	-
80502325008	-	-	$2.80^{+0.04}_{-0.05}$...	1.0^*	$1.681^{+0.003}_{-0.003}$	$3.18^{+0.03}_{-0.04}$...	400^*	$0.256^{+0.006}_{-0.005}$	$28.9^{+0.4}_{-0.2}$	-	-
90401369004	-	-	0.0^*	...	1.0^*	$1.581^{+0.001}_{-0.002}$	$1.91^{+0.12}_{-0.09}$...	$90.3^{+3.1}_{-2.1}$	$0.160^{+0.003}_{-0.005}$	$43.0^{+0.7}_{-0.7}$	-	-
H1743-322 ^(d)													

Table 3. continued.

ObsID	T_{in} (keV)	N_{disk}	q	i (deg.)	R_{in} (R_g)	Γ	$\log \xi$	A_{Fe}	kT_e (keV)	R_f	N_{rel} ($\times 10^{-4}$)	N_{tot} ($\times 10^{-4}$)	χ^2/ν
80001044002	-	-	2.7 ^{+1.5} _{-0.6}	51.9 ^{+2.0} _{-5.6}	4.4 ^{+1.2} _{-0.6}	1.642 ^{+0.006} _{-0.006}	1.8 ^{+0.1} _{-0.1}	0.5*	150.1 ^{+4.9} _{-9.7}	0.34 ^{+0.03} _{-0.10}	76.0 ^{+1.6} _{-1.3}	-	-
80001044004	-	-	2.3 ^{+0.3} _{-0.2}	...	4.2 ^{+0.5} _{-0.7}	1.690 ^{+0.006} _{-0.006}	2.0 ^{+0.1} _{-0.1}	...	88.9 ^{+7.3} _{-12.5}	0.38 ^{+0.03} _{-0.06}	85.2 ^{+1.3} _{-1.2}	-	-
80001044006	-	-	1.9 ^{+0.2} _{-0.3}	...	8.3 ^{+0.7} _{-3.1}	1.690 ^{+0.009} _{-0.011}	1.4 ^{+0.5} _{-0.2}	...	76.8 ^{+6.8} _{-7.0}	0.43 ^{+0.03} _{-0.06}	73.8 ^{+1.6} _{-1.6}	-	-
80002040002	-	-	2.2 ^{+0.3} _{-0.4}	...	6.9 ^{+0.8} _{-1.2}	1.630 ^{+0.012} _{-0.008}	0.1*	...	290.0 ^{+19.9} _{-18.5}	0.29 ^{+0.05} _{-0.04}	57.2 ^{+1.5} _{-1.9}	-	12438.6 12080
80202012002	-	-	1.1 ^{+0.6} _{-0.3}	...	2.6 ^{+1.4} _{-1.0}	1.848 ^{+0.026} _{-0.009}	1.7 ^{+0.2} _{-0.0}	...	66.9 ^{+7.6} _{-3.5}	0.42 ^{+0.13} _{-0.04}	80.4 ^{+0.7} _{-2.9}	-	-
80202012004	-	-	2.3 ^{+0.7} _{-0.5}	...	3.8 ^{+1.2} _{-0.6}	1.864 ^{+0.027} _{-0.007}	1.5 ^{+0.1} _{-0.1}	...	158.4 ^{+5.2} _{-5.4}	0.42 ^{+0.11} _{-0.04}	81.5 ^{+0.8} _{-2.9}	-	-
80202012006	-	-	2.5 ^{+0.2} _{-0.1}	...	3.9 ^{+0.5} _{-0.4}	1.661 ^{+0.006} _{-0.007}	0.1*	...	178.5 ^{+94.4} _{-25.8}	0.27 ^{+0.03} _{-0.04}	57.5 ^{+1.9} _{-1.4}	-	-
90401335002	-	-	1.9 ^{+0.1} _{-0.2}	...	6.5 ^{+0.6} _{-1.7}	1.704 ^{+0.010} _{-0.020}	1.7 ^{+0.1} _{-0.1}	...	72.0 ^{+5.3} _{-2.9}	0.31 ^{+0.05} _{-0.15}	78.4 ^{+5.2} _{-1.9}	-	-
IGR J17091-3624 ^(d)													
80001041002	-	-	2.2 ^{+0.5} _{-0.3}	52.3 ^{+7.3} _{-10.0}	7.6 ^{+7.6} _{-4.9}	1.739 ^{+0.009} _{-0.009}	1.3 ^{+0.6} _{-0.5}	0.5*	400*	0.56 ^{+0.12} _{-0.11}	39.0 ^{+0.9} _{-0.9}	-	-
80202014002	-	-	2.7 ^{+1.8} _{-0.5}	...	13.2 ^{+20.1} _{-9.6}	1.737 ^{+0.014} _{-0.013}	2.5 ^{+0.1} _{-0.1}	...	54.7 ^{+12.4} _{-8.6}	0.40 ^{+0.18} _{-0.10}	42.1 ^{+1.1} _{-1.2}	-	3128.1 3603
80202014004	-	-	1.8 ^{+0.5} _{-0.7}	...	10.1 ^{+10.0} _{-6.2}	1.740 ^{+0.009} _{-0.008}	2.6 ^{+0.1} _{-0.1}	...	36.7 ^{+5.4} _{-3.7}	0.26 ^{+0.05} _{-0.05}	45.3 ^{+0.8} _{-0.8}	-	-
MAXI J1348-630 ^(a)													
80402315002	0.50 ^{+0.01} _{-0.01}	16290.3 ^{+1737.6} _{-2093.8}	2.2 ^{+0.2} _{-0.1}	17.3 ^{+1.1} _{-1.5}	4.0 ^{+0.8} _{-0.4}	1.687 ^{+0.003} _{-0.003}	3.58 ^{+0.03} _{-0.03}	2.1 ^{+0.1} _{-0.1}	25.5 ^{+1.3} _{-0.8}	0.18 ^{+0.02} _{-0.01}	1930.9 ^{+19.3} _{-17.7}	-	-
80402315004	0.53 ^{+0.03} _{-0.01}	9955.0 ^{+639.8} _{-1094.3}	10.0*	...	16.1 ^{+2.5} _{-3.5}	1.688 ^{+0.004} _{-0.006}	3.45 ^{+0.05} _{-0.03}	...	23.3 ^{+1.3} _{-1.2}	0.17 ^{+0.02} _{-0.01}	1952.1 ^{+20.9} _{-28.4}	-	-
80502304002	0.58 ^{+0.02} _{-0.01}	744.8 ^{+136.4} _{-60.1}	2.6 ^{+0.1} _{-0.1}	...	3.5 ^{+0.5} _{-0.2}	1.644 ^{+0.018} _{-0.005}	3.43 ^{+0.06} _{-0.23}	...	89.6 ^{+11.7} _{-9.4}	0.25 ^{+0.01} _{-0.03}	444.5 ^{+30.9} _{-16.7}	-	7810.4 7131
80502304004	0.54 ^{+0.01} _{-0.01}	1209.0 ^{+52.2} _{-145.3}	3.1 ^{+0.5} _{-0.2}	...	7.8 ^{+2.0} _{-2.0}	1.639 ^{+0.008} _{-0.004}	3.21 ^{+0.04} _{-0.09}	...	80.3 ^{+17.8} _{-14.3}	0.16 ^{+0.01} _{-0.01}	419.7 ^{+15.7} _{-11.7}	-	-
80502304006	0.59 ^{+0.01} _{-0.02}	335.3 ^{+96.6} _{-38.7}	2.4 ^{+0.1} _{-0.1}	...	5.9 ^{+1.9} _{-1.2}	1.637 ^{+0.005} _{-0.010}	3.09 ^{+0.07} _{-0.07}	...	89.5 ^{+3.1} _{-3.6}	0.16 ^{+0.03} _{-0.01}	287.5 ^{+3.9} _{-4.8}	-	-
MAXI J1535-571 ^(c)													
90301013002	0.40 ^{+0.01} _{-0.01}	217048.3 ^{+50274.2} _{-36802.9}	5.9 ^{+3.1} _{-3.6}	56.4 ^{+6.7} _{-2.5}	3.3 ^{+0.7} _{-0.9}	1.83 ^{+0.04} _{-0.04}	3.7 ^{+0.2} _{-0.3}	1.2 ^{+0.8} _{-0.5}	19.7 ^{+1.7} _{-0.7}	0.77 ^{+0.15} _{-0.13}	863.5 ^{+107.2} _{-122.6}	111.9 ^{+53.7} _{-33.3}	1747.4 1671
80402303002	-	-	3.7 ^{+3.0} _{-1.1}	17.9 ^{+5.9} _{-6.9}	7.5 ^{+6.2} _{-3.7}	1.61 ^{+0.01} _{-0.02}	3.4 ^{+0.3} _{-0.2}	1.5 ^{+0.4} _{-0.3}	400*	0.15 ^{+0.06} _{-0.03}	49.1 ^{+1.8} _{-3.2}	-	-
80402303004	-	-	3.9 ^{+2.3} _{-1.1}	...	7.4 ^{+6.9} _{-3.2}	1.65 ^{+0.01} _{-0.01}	2.8 ^{+0.2} _{-0.2}	...	307.2 ^{+59.7} _{-76.8}	0.12 ^{+0.03} _{-0.02}	41.2 ^{+1.2} _{-1.4}	-	2812.0 3322
80402303006	-	-	6.2 ^{+2.6} _{-2.4}	...	14.9 ^{+6.0} _{-4.5}	1.69 ^{+0.01} _{-0.01}	3.1 ^{+0.1} _{-0.1}	...	400*	0.15 ^{+0.03} _{-0.02}	39.4 ^{+0.7} _{-0.9}	-	-
MAXI J1820+070 ^(c)													
90401309002	1.5*	4.6 ^{+0.1} _{-0.1}	10.0*	63 [†]	207.7 ^{+4.0} _{-3.3}	1.510 ^{+0.001} _{-0.001}	0.1*	2.47 ^{+0.04} _{-0.04}	40.6 ^{+0.6} _{-0.5}	0.13 ^{+0.00} _{-0.00}	525.7 ^{+2.9} _{-2.9}	33.2 ^{+1.0} _{-1.2}	-
90401309004	1.5*	26.0 ^{+0.8} _{-0.9}	2.0 ^{+0.1} _{-0.1}	...	2.9 ^{+0.0} _{-0.0}	1.640 ^{+0.002} _{-0.002}	1.98 ^{+0.02} _{-0.01}	...	39.7 ^{+0.9} _{-0.9}	0.54 ^{+0.03} _{-0.01}	1628.1 ^{+12.2} _{-14.7}	0.1*	-
90401309006	1.21 ^{+0.01} _{-0.01}	84.1 ^{+2.4} _{-2.1}	2.0 ^{+0.1} _{-0.1}	...	12.7 ^{+0.5} _{-0.3}	1.577 ^{+0.001} _{-0.001}	3.20 ^{+0.02} _{-0.01}	...	24.4 ^{+0.6} _{-0.7}	0.21 ^{+0.01} _{-0.01}	1536.1 ^{+12.9} _{-13.7}	180.1 ^{+4.8} _{-4.7}	-
90401309008	0.73 ^{+0.01} _{-0.01}	598.2 ^{+12.5} _{-12.1}	1.7 ^{+0.1} _{-0.1}	...	19.1 ^{+0.3} _{-0.4}	1.591 ^{+0.002} _{-0.002}	3.80 ^{+0.02} _{-0.04}	...	43.3 ^{+1.3} _{-1.2}	0.81 ^{+0.05} _{-0.03}	1256.3 ^{+15.7} _{-14.8}	300.0 ^{+6.2} _{-5.9}	-
90401309010	0.96 ^{+0.02} _{-0.01}	147.5 ^{+3.6} _{-4.5}	2.1 ^{+0.1} _{-0.1}	...	25.1 ^{+0.6} _{-0.7}	1.567 ^{+0.002} _{-0.001}	3.90 ^{+0.01} _{-0.01}	...	42.5 ^{+1.1} _{-1.4}	1.32 ^{+0.02} _{-0.02}	996.9 ^{+11.0} _{-12.9}	318.4 ^{+9.5} _{-8.6}	-
90401309012	1.08 ^{+0.01} _{-0.01}	113.8 ^{+4.6} _{-3.4}	2.4 ^{+0.1} _{-0.1}	...	17.3 ^{+0.5} _{-0.5}	1.595 ^{+0.002} _{-0.003}	3.25 ^{+0.01} _{-0.01}	...	29.7 ^{+0.7} _{-0.6}	0.23 ^{+0.00} _{-0.01}	1464.5 ^{+9.9} _{-12.7}	144.1 ^{+1.8} _{-1.7}	-
90401309013	0.63 ^{+0.01} _{-0.01}	875.6 ^{+31.2} _{-24.5}	2.0 ^{+0.0} _{-0.0}	...	3.6 ^{+0.1} _{-0.1}	1.728 ^{+0.003} _{-0.002}	1.74 ^{+0.04} _{-0.02}	...	79.7 ^{+3.6} _{-2.0}	0.73 ^{+0.02} _{-0.02}	1555.8 ^{+10.4} _{-9.8}	0.7 ^{+0.0} _{-0.0}	-
90401309014	1.03 ^{+0.01} _{-0.01}	138.6 ^{+5.2} _{-3.8}	2.8 ^{+0.1} _{-0.1}	...	18.2 ^{+0.9} _{-0.9}	1.623 ^{+0.001} _{-0.001}	3.24 ^{+0.01} _{-0.02}	...	31.6 ^{+0.8} _{-1.0}	0.26 ^{+0.01} _{-0.01}	1383.7 ^{+10.2} _{-11.7}	137.5 ^{+4.8} _{-5.2}	-
90401309016	0.53 ^{+0.01} _{-0.01}	2974.1 ^{+107.1} _{-117.7}	10.0*	...	27.0 ^{+1.0} _{-1.1}	1.651 ^{+0.003} _{-0.002}	3.73 ^{+0.02} _{-0.01}	...	133.1 ^{+3.1} _{-3.0}	0.84 ^{+0.02} _{-0.02}	1029.4 ^{+10.4} _{-15.7}	169.6 ^{+3.6} _{-5.2}	-
90401309018	0.87 ^{+0.03} _{-0.02}	182.5 ^{+7.9} _{-6.1}	2.2 ^{+0.1} _{-0.1}	...	11.1 ^{+0.4} _{-0.4}	1.677 ^{+0.002} _{-0.002}	3.35 ^{+0.02} _{-0.02}	...	53.7 ^{+1.7} _{-1.9}	0.40 ^{+0.01} _{-0.01}	1034.1 ^{+1.1} _{-1.1}	62.8 ^{+1.9} _{-1.8}	-
90401309019	0.73 ^{+0.01} _{-0.01}	462.7 ^{+17.1} _{-12.1}	10.0*	...	22.1 ^{+0.8} _{-0.8}	1.678 ^{+0.001} _{-0.001}	3.51 ^{+0.02} _{-0.01}	...	96.0 ^{+3.4} _{-4.3}	0.58 ^{+0.02} _{-0.02}	991.9 ^{+10.6} _{-7.5}	135.9 ^{+3.4} _{-2.9}	-

Table 3. continued.

ObsID	T_{in} (keV)	N_{disk}	q	i (deg.)	R_{in} (R_g)	Γ	$\log \xi$	A_{Fe}	kT_e (keV)	R_f	N_{rel} ($\times 10^{-4}$)	N_{xit} ($\times 10^{-4}$)	χ^2/ν
90401309021	$0.74^{+0.01}_{-0.01}$	$287.8^{+5.1}_{-4.8}$	$2.6^{+0.2}_{-0.1}$...	$12.5^{+0.4}_{-0.5}$	$1.649^{+0.002}_{-0.001}$	$3.23^{+0.01}_{-0.01}$...	$262.7^{+4.6}_{-4.8}$	$0.37^{+0.02}_{-0.01}$	$843.9^{+6.0}_{-9.1}$	$54.2^{+1.3}_{-1.6}$	
90401309033	$0.70^{+0.01}_{-0.01}$	$406.4^{+35.0}_{-38.5}$	$3.2^{+0.3}_{-0.2}$...	$8.1^{+0.9}_{-0.6}$	$1.880^{+0.003}_{-0.003}$	$3.33^{+0.03}_{-0.02}$...	400*	$0.78^{+0.05}_{-0.04}$	$203.9^{+3.4}_{-4.7}$	$10.3^{+2.0}_{-2.1}$	
90401309035	$1.32^{+0.05}_{-0.03}$	$1.9^{+0.3}_{-0.2}$	10.0*	...	$52.8^{+9.3}_{-6.8}$	$1.660^{+0.005}_{-0.006}$	$2.90^{+0.07}_{-0.07}$...	$228.4^{+24.2}_{-17.7}$	$0.15^{+0.01}_{-0.02}$	$156.0^{+2.0}_{-1.9}$	$3.5^{+0.7}_{-0.5}$	
90401309037	-	-	10.0*	...	$63.3^{+9.8}_{-10.8}$	$1.730^{+0.005}_{-0.006}$	$2.91^{+0.08}_{-0.10}$...	400*	$0.16^{+0.02}_{-0.02}$	$38.1^{+0.4}_{-0.4}$	$2.1^{+0.3}_{-0.2}$	$\frac{7878.0}{7307}$
90401324002	$0.80^{+0.02}_{-0.02}$	$271.6^{+36.1}_{-29.8}$	10.0*	...	$21.7^{+2.8}_{-1.8}$	$1.685^{+0.004}_{-0.004}$	$3.46^{+0.05}_{-0.04}$...	$82.5^{+10.4}_{-9.1}$	$0.49^{+0.04}_{-0.04}$	$986.5^{+29.6}_{-23.5}$	$112.6^{+10.4}_{-11.0}$	
90501311002	-	-	10.0*	...	$112.4^{+17.9}_{-20.6}$	$1.723^{+0.005}_{-0.005}$	$2.85^{+0.10}_{-0.10}$...	$80.0^{+11.6}_{-12.6}$	$0.12^{+0.01}_{-0.02}$	$32.8^{+0.6}_{-0.9}$	$3.1^{+0.6}_{-0.4}$	
90501337002	-	-	10.0*	-	400.0*	$1.706^{+0.004}_{-0.005}$	$2.71^{+0.06}_{-0.09}$...	$133.6^{+17.3}_{-15.3}$	$0.15^{+0.02}_{-0.02}$	$37.5^{+0.6}_{-0.6}$	$3.0^{+0.4}_{-0.6}$	
Swift J1753.5-0127 ^(b)													
30001148002	-	-	-	-	-	$1.736^{+0.004}_{-0.004}$	-	-	> 55.8	-	-	-	$\frac{1069.5}{987}$

Note:

- The letter 'a' indicates the spectral model TBabs*(diskbb+relxillcp) adopted in the sources.
- The letter 'b' indicates the spectral model TBabs*nthcomp adopted in the sources.
- The letter 'c' indicates the spectral model TBabs*(diskbb+relxillcp+xiilvercp) adopted in the sources.
- The letter 'd' indicates the spectral model TBabs*relxillcp adopted in the sources.
- The symbol '*' indicates the parameters are pegged at lower/upper limit adopted in the spectral fits.
- The symbol '+' indicates the parameters are fixed at the values given in Table 1.
- The symbol '-' indicates the parameters are linked in the joint fits for a given source.
- The symbol '.' for T_{in} and N_{disk} in the diskbb model indicates that the disk component is not required in the fits for a given observation. $T_{\text{in}} = 0.05$ keV and $N_{\text{disk}} = 10^{-5}$ are fixed in the joint fits.

APPENDIX

A. COMPARISON WITH THE EXISTING CONSTRAINTS

A.1. *GRS 1716-249*

The spectral analysis for the four epochs, i.e., 80201034006, 80201034007, 90202055002, and 90202055004, was also done by Jiang et al. (2020). In their spectral fits, the power-law model `cutoffpl` is used to account for the coronal emission, and the `relconvlp*reflionx` is adopted to model the relativistic disk reflection, where `kerrconv` is a relativistic blurring function based on ray-tracing simulations (Brenneman & Reynolds 2006) and `reflionx` accounts for the reflection from an ionized accretion disk of constant density (Ross & Fabian 2005). Their results show that the inclination angle is low with $i \sim 30^\circ$, and the accretion disk is of low iron abundance and highly ionized, which are consistent with our results. The Comptonization continua are harder with the photon index in the range of 1.3-1.5 than the ones in our fitting results, and the reflection fraction is about 0.25. Note that, the modeling of the relativistic disk reflection with `relconvlp*reflionx` is based on the assumption of a simple lamppost geometry, and more importantly, the empirical reflection fraction in `relconvlp*reflionx` is different from the physical reflection fraction in the reflection model `relxillCp` adopted in our work (Dauser et al. 2016).

A.2. *GRS 1739-278*

The four *NuSTAR* spectra of GRS 1739-278 studied in this work are well described by a power-law continuum with an exponential cutoff, which agrees with the results in previous studies (Fürst et al. 2016; Yan et al. 2020). Joint fits of *XMM-Newton* and *NuSTAR* for one epoch observation on MJD 57281 (ObsID: 80101050002) by Fürst et al. (2016) revealed the signatures of reflection. Their spectral fits indicate a low reflection fraction with $R = 0.043$ for a hard spectrum with photon index $\Gamma = 1.39$, which agrees well with the low end of the R - Γ correlation.

A.3. *GRS 1915+105*

The *NuSTAR* spectrum of GRS 1915+105 in 2012 (ObsID: 10002004001) was analyzed in previous studies with the reflection model (`kerrconv*reflionx`)+`cutoffpl`. In Miller et al. (2013), the spectral model mainly consists of (`kerrconv*reflionx`)+`cutoffpl`. Assuming the disk inner edge being at ISCO, their best fits prefer a high BH spin with $a = 0.98$ and a large inclination angle for this binary system with $i = 72^\circ$, and strongly exclude the fitting results with a much high cutoff energy. As a comparison, in our fits of this observation with the assumptions of $a = 0.998$ and $i = 60^\circ$, the fitted inner radius of the disk is about $2 R_{\text{ISCO}}$, and the electron temperature kT_e is about 17 keV. However, the derived photon index in our fits is about 1.9, which is larger than the one (~ 1.7) in Miller et al. (2013). The same observation was also studied using the relativistic reflection models `relxill_NK` (Bambi et al. 2017) which belongs to the RELXILL family (Zhang et al. 2019a,b; Shreeram & Ingram 2020). The fitted photon index in those studies is large with $\Gamma = 2.13$, instead.

A.4. *GS 1354-64*

The three *NuSTAR* spectra of GS 1354-64 were analyzed by Yan et al. (2020) in which the Comptonization model (`nthcomp`) is adopted, while the disk reflection is not included, for simplicity. In their spectral fits, the photon index of the Comptonization continuum is $\Gamma = 1.49, 1.57, 1.65$, and the fitted electron temperature is low with $kT_e \sim 10\text{--}20$ keV, which are consistent with the results in this work.

Moreover, two of the three *NuSTAR* spectra (ObsID: 90101006002, 90101006004), were also analyzed in previous studies with the reflection model (El-Batal et al. 2016; Xu et al. 2018a; Tripathi et al. 2021). El-Batal et al. (2016) found a large truncation radius for the accretion disk with $R_{\text{in}} = 700^{+200}_{-500} R_{\text{ISCO}}$ for 90101006002, but a small truncation radius, which is close to R_{ISCO} for 90101006004. In this work, we also find the similar results that the disk is truncated at a large radius with $R_{\text{in}} \approx 44^{+37}_{-17} R_{\text{ISCO}}$ for 90101006002, but at a small radius $R_{\text{in}} = 9.8^{+11.8}_{-8.3} R_{\text{ISCO}}$ for 90101006004. And a low iron abundance with $A_{\text{Fe}} \sim 0.5$ is preferred in both El-Batal et al. (2016) and our work.

A.5. *GX 339-4*

The *NuSTAR* spectra of GX 339-4 studied in this work mainly consist of the observations in 2013 (Fürst et al. 2015; Wang-Ji et al. 2018; Jiang et al. 2019), 2015 (Wang-Ji et al. 2018; Jiang et al. 2019), and 2017 (García et al. 2019; Wang et al. 2020a). For the observations in 2013 (ObsID: 80001013002-04-06-08-10) and 2015 (ObsID: 80102011002-04-06-10-12), the reflection models in the `relxill` family are implemented by Wang-Ji et al. (2018) in the joint fits to *NuSTAR* and *Swift* data. In their

results, the inclination angle is constrained with $i \sim 40^\circ$, which supports the assumption of the inclination angle in our fits. And the electron temperatures are found to be large with $kT_e \sim$ hundreds of kiloelectronvolts and the disk inner radii are close to the ISCO, which are consistent with our fitting results. The constrained photon index is in the range of 1.5-1.7, as we find in this work. And both Wang-Ji et al. (2018) and our work found that the spectra prefers to a high iron abundance. Note that, such a high iron overabundance may be due to the assumed constant electron density of the accretion disk $n_e = 10^{15} \text{ cm}^{-3}$ (Jiang et al. 2019).

A.6. H1743-322

The *NuSTAR* spectra of H1743-322 were also analyzed with the phenomenological models (Yan et al. 2020; Wang et al. 2022) and the reflection models in the *relxill* family (Ingram et al. 2016; Chand et al. 2020; Stiele & Kong 2021). A low iron abundance with $A_{\text{Fe}} \sim 0.5$ and a small disk truncation radius of a few times R_{ISCO} are suggested in the spectral fits (Ingram et al. 2016; Stiele & Kong 2021). And the fitted photon index and the reflection fraction by Stiele & Kong (2021) follow the derived correlation in this work.

A.7. IGR J17091-3624

The *NuSTAR* spectra of IGR J17091-3624 were analyzed by Xu et al. (2017) with the reflection models in the *relxill* family. In their spectral results, the constrained inner radii are about of tens of gravitational radii, and the iron abundance is low with $A_{\text{Fe}} \sim 0.7$, which are consistent with the results in this work. And the fitted photon index and the reflection fraction are slightly lower than the ones in our results.

A.8. MAXI J1348-630

Two of the *NuSTAR* spectra of MAXI J1348-630 studied in this work (ObsIDs: 80402315002 and 80402315004) were also analyzed in Chakraborty et al. (2021) and Jia et al. (2022) with the reflection models in the *relxill* family. In their results, the disk temperature at the inner radius is about 0.5 keV. For the Comptonizing source, the photon index $\Gamma \sim 1.7$, and the electron temperature $kT_e \sim 30$ keV. These measurements are consistent with the ones in this work. We notice that the disk in their fits is truncated at $\sim 10R_g$, while the inner radius in our results is about $\sim 5R_g$. Furthermore, their reflection fraction is slightly smaller than the one in our fits.

A.9. MAXI J1535-571

The *NuSTAR* spectra of MAXI J1348-630 were analyzed by Xu et al. (2018b) and Dong et al. (2022). The observation (ObsID = 90301013002) was fitted by Xu et al. (2018b) with different flavors of the reflection models in the *relxill* family. Our fitting results, in terms of the disk properties (the inner temperature kT_{bb} , iron abundance, and the ionization parameter), the Comptonization spectrum (the electron temperature kT_e and the photon index), and the reflection fraction, are consistent with the ones in Xu et al. (2018b).

A.10. MAXI J1813-095

The three *NuSTAR* spectra of MAXI J1813-095 were stacked by Jiang et al. (2022) for the spectral analysis with the reflection models in the *relxill* family. In their results, the inclination of the source is found to be low with $i \sim 22^\circ$ which supports our conclusion of a low inclination angle of $i \sim 18^\circ$. And, the disk properties (the inner temperature T_{in} , iron abundance, and the ionization parameter), the Comptonization spectrum (the electron temperature kT_e and the photon index) in our fits are consistent with the ones in Jiang et al. (2022).

A.11. MAXI J1820+070

The *NuSTAR* spectra of MAXI J1820+070 in the 2018 outburst were analyzed by Buisson et al. (2019) with a dual-lamppost model (two lampposts at different coronal heights) *relxilllpCp* in the *relxill* family. In their results, the inclination angle is fitted to be $\sim 30^\circ$, while it is fixed with $i = 63^\circ$ (Atri et al. 2020) in this work. Note that there is a large misalignment ($> 40^\circ$) between the inclination angle of the jet and the binary orbit in MAXI J1820+070 (Poutanen et al. 2022).

A.12. Swift J1753.5-0127

The *NuSTAR* spectra of Swift J1753.5-0127 studied in this work are well-described by a power-law continuum with an exponential cutoff. The Comptonization spectrum, in terms of the electron temperature kT_e and the photon index, in our fits are consistent with the results in previous studies (Yan et al. 2020), which include the *Swift* data as well.